Efficient sliding locomotion of three-link bodies

Silas Alben*
Department of Mathematics, University of Michigan, Ann Arbor, Michigan 48109, USA

(Received 6 December 2020; revised 19 February 2021; accepted 22 March 2021; published 16 April 2021)

We study the efficiency of sliding locomotion for three-link bodies with prescribed joint angle motions. The bodies move with no inertia, under dry (Coulomb) friction that is anisotropic (different in the directions normal and tangent to the links) and directional (different in the forward and backward tangent directions). Friction coefficient space can be partitioned into several regions, each with distinct types of efficient kinematics. These include kinematics resembling lateral undulation with very anisotropic friction, small-amplitude reciprocal kinematics, very large-amplitude kinematics near isotropic friction, and kinematics that are very asymmetric about the flat state. In the two-parameter shape space, zero net rotation for elliptical trajectories occurs mainly with bilateral or antipodal symmetry. These symmetric subspaces have about the same peak efficiency as the full space but with much smaller dimension. Adding the second or third harmonics greatly increases the numbers of local optimal for efficiency, but only modestly increases the peak efficiency. Random ensembles with higher harmonics have efficiency distributions that peak near a certain nonzero value and decay rapidly up to the maximum efficiency. A stochastic optimization algorithm is developed to compute optima with higher harmonics. These are simple closed curves, sharpened versions of the elliptical optima in most cases, and achieve much higher efficiencies mainly for small normal friction. With a linear (viscous) resistance law, the optimal trajectories are similar in much of the friction coefficient space, and relative efficiencies are much lower except with very large normal friction.

DOI: 10.1103/PhysRevE.103.042414

I. INTRODUCTION

In this work, we investigate sliding locomotion by three-link bodies. Such bodies are a benchmark system for studying the basic physics of locomotion for swimming microorganisms [1–13] and other locomoting bodies [14–16]. With only three links (and thus only two internal degrees of freedom, the interlink angles), it is easier to consider the full range of possible motions. The low-dimensional configuration space also facilitates optimization studies by limiting the space of possible motions, and therefore perhaps the number of local minima in the optimized quantity (typically efficiency—defined here as the average speed divided by the average input power). Three links are enough to approximate perhaps the most common swimming and crawling motions: undulatory traveling-wave motions [1,17]. With two links, time-periodic motions are limited to reciprocal, scallop-type motions. Here locomotion is possible with fore-aft frictional anisotropy [15], buoyancy [18], change of shape [19], or when body inertia is considered for sliding bodies [20], in which case it may be relatively efficient. The main assumptions of this work—anisotropic resistance forces, negligible body inertia, and prescribed joint angles—are common to most previous studies of n-link microswimmers and crawling bodies mentioned here.

By considering bodies with more than three links [9,22–24], studies have obtained some of the benefits of simplifying the body's spatial configuration while approaching the case of a smooth body. In an earlier work, we computed the optimally efficient sliding motions of a smooth curvilinear body using a quasi-Newton local optimization algorithm starting from various random initial points in the space of time-periodic body kinematics [21]. We truncated the number of shape degrees of freedom at 45 in most cases, superposing products of five spatial modes with nine temporal modes. We computed optima across a space of friction anisotropy ratios (shown in Fig. 1), i.e., the ratios of friction coefficients for sliding in the normal direction (values on the horizontal axis) and the backward direction (values on the vertical axis), relative to the coefficient of friction in the forward direction, which is generally the smallest for real snakes [25]. Here forward and backward sliding means sliding tangent to the body axis (or backbone) in the direction of the head or tail, respectively, and normal sliding means sliding perpendicular to the body axis, to either side. The model originated in previous experimental and theoretical studies of snake and snake-robot locomotion [25–29], analogous to resistive force theory for swimmers [17,30]. Many of the optimal motions found in Ref. [21] could be classified as direct, retrograde, or standing waves of body axis curvature, based on whether the local curvature maxima propagate toward or away from the direction of locomotion, or remain stationary, respectively. In the rightmost portion of the parameter space in Fig. 1 we have $\mu_n/\mu_f \gg 1$, a common regime for snakes and snake robots [31,32]. Here the optimally efficient motions are relatively smooth retrograde traveling-wave motions, and they are relatively unchanged when the number of spatial and temporal degrees of freedom in the body kinematics are approximately doubled (from 5 to 10, and 9 to 19, respectively). In the limit $\mu_n/\mu_f \to \infty$, the retrograde waves can achieve the upper

*alben@umich.edu

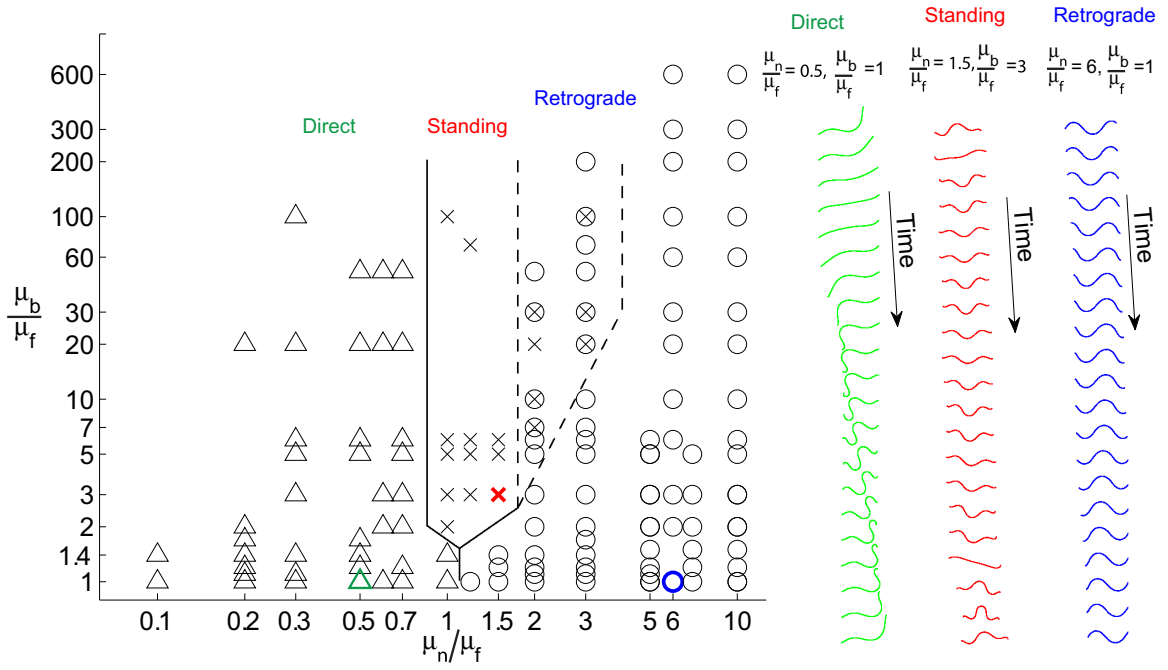

FIG. 1. Left: Classification of local optima across friction coefficient space, presented in [21]. The triangles, crosses, and circles mark locations where optima that are direct, standing, or retrograde waves were found, respectively. The solid lines mark interfaces between regions containing a distinct type of wave optimum, while the dashed lines delineate a region with both standing- and retrograde-wave optima. Right: Three sequences of snapshots of locally optimal motions giving examples of direct, standing, and retrograde waves. These occur at particular friction coefficient ratios, listed above the snapshots and marked with green, red, and blue symbols in the panel at left. The three sequences of snapshots are given over one period of motion, and they are displaced vertically to enhance visibility, but the actual net displacement is horizontal.

bound for efficiency, corresponding to uniform sliding in the direction of lowest friction [21]. The case $\mu_n/\mu_f = +\infty$, corresponding to bodies mounted on knife edges or no-skid wheels [33], can result in kinematic singularities that may be resolved physically by wheel slippage [16]. The central part of the parameter space in Fig. 1, $\mu_n/\mu_f \approx 1$ and $\mu_b/\mu_f \geqslant 1$, includes two other common regimes for biological snakes: isotropic friction and larger backward friction (due to snake scales). Here standing-wave optima were found in [21]. The left part of Fig. 1, $\mu_n/\mu_f < 1$, can be realized in wheeled snake robots by turning the wheels 90°, so the wheel axis of rotation is along the body tangent, and the wheels roll along the body normal. Here direct wave motions were among the local optima identified in [21]. In the central and left regions of Fig. 1 there were many optima that were difficult to classify, and it was difficult to obtain convergence from many of the random initial conditions, and to identify global optima. Therefore, in this work we limit the number of spatial degrees of freedom by considering three-link bodies. One advantage is easier visualization of the trajectories in the space of body shapes, which is two-dimensional. With fewer degrees of freedom, optimization is also easier, and we can more completely describe local optima throughout friction coefficient space. Another advantage is that we can go beyond optimization and describe the entire space of possible kinematics to some extent, not just the kinematics that are optimally efficient. At the end of the paper, we employ a stochastic optimization algorithm, which has some robustness advantages over that in [21], to compute optimal three-link kinematics with many temporal modes. We also use it to compute optimal three-link motions with a linear resistance law, corresponding to swimming in or sliding on a viscous medium, and we compare with the optima for dry-friction resistance. In [15], we computed optimal kinematics of three-link bodies with up to two harmonics, at a particular choice of friction coefficient ratios motivated by the experiments in [29]. Fast computations of locomotion without inertia are facilitated by precomputing "velocity maps," i.e., maps from shape change to displacements and rotations in physical space [14,15,34]. In [34–36], velocity maps were used to predict swimming motions that give large net displacements with zero net rotation. In [37], we developed the iterative method for computing velocity maps with Coulomb friction resistance that is used here, and we computed optimal motions of three-link bodies with isotropic friction and a single harmonic. Now, we develop a stochastic optimization algorithm that allows us to compute optimal kinematics with many harmonics (up to nine are used here) in a large portion of the two-dimensional space of friction coefficient ratios. We also describe the properties of the full space of kinematics, both optimal and nonoptimal. Among the alternatives to the continuous and stochastic optimization methods we have used are geometric variational formulations [11,38,39], which provide additional geometric insights into the properties of the optima.

The overall goal in this paper is to describe the range of possibilities for sliding motions across friction coefficient space more thoroughly than has been done previously, with an emphasis on those that are optimally efficient, locally and

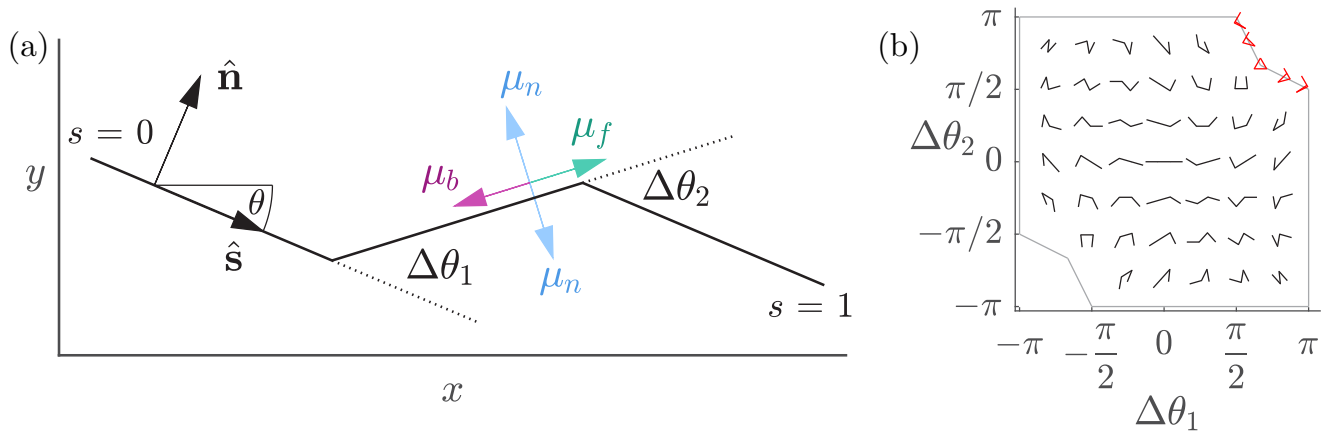

FIG. 2. (a) Schematic diagram of a three-link body with changes in angles $\Delta\theta_1$ (here positive) and $\Delta\theta_2$ (here negative) between the links. The body is parametrized by arc length s (nondimensionalized by body length) at an instant in time. The tangent angle and the unit vectors tangent and normal to the curve at a point are labeled. Vectors representing forward, backward, and normal velocities are shown with the corresponding friction coefficients μ_f, μ_b, and μ_n. (b) Examples of body shapes in the $(\Delta\theta_1, \Delta\theta_2)$-plane. Shapes that do not self-intersect are shown in black; a few shapes at the threshold of self-intersection are shown in red.

globally. This is made possible by restricting to the case of three-link bodies. In Sec. II, we briefly review the model, which is the same as in many previous studies. We then restrict to single-harmonic (elliptical) trajectories in Sec. III, and we define 10 clusters that represent the typical optimal motions that occur across friction coefficient space. The optima with the highest relative efficiency occur with a large backward friction coefficient and the normal and forward friction coefficients about equal. Those with the lowest relative efficiency occur when the ratio of normal to forward friction coefficients is very small or large. We find that symmetric motions achieve efficiencies as high as nonsymmetric motions in most cases. In Sec. IV, we consider the spaces of trajectories with up to three harmonics. They allow large increases in efficiency near isotropic friction, and in regions with either small normal friction coefficients or large backward friction coefficients. In Sec. V, we employ a stochastic optimization method to find efficiency-optimizing trajectories with up to nine harmonics. Over friction coefficient space, about six types of motions are seen, and the improvement over the elliptical trajectories is largest when the normal friction coefficient is small. With a viscous resistance model, the optima are qualitatively similar to those with Coulomb friction when the resistance coefficients have moderate-to-large anisotropy. Section VI summarizes the results.

II. MODEL

We use the same Coulomb-friction model as [15,25,29] and other recent studies. The body is thin compared to its length, so for simplicity we approximate its motion by that of a polygonal curve $\mathbf{X}(s,t) = (x(s,t), y(s,t))$, parametrized by arc length s and varying with time t. A schematic diagram is shown in Fig. 2(a).

The basic problem is to prescribe the time-dependent shape of the body in order to obtain efficient locomotion. The shape is described by $\Delta\theta_1(t)$ and $\Delta\theta_2(t)$, the differences between the tangent angles of the adjacent links. A set of possible body shapes is plotted at the corresponding $(\Delta\theta_1, \Delta\theta_2)$ locations in Fig. 2(b). The region inside the gray polygonal boundary consists of shapes that do not self-intersect. Five examples of shapes that lie on the boundary are shown in red (along the upper right portion of the boundary). In this work, we will consider time-periodic kinematics, which are represented by closed curves in the $(\Delta\theta_1, \Delta\theta_2)$-plane.

To write the dynamical equations (Newton's laws), we first write the body tangent angle as $\theta(s,t)$; it satisfies $\partial_s x = \cos\theta$ and $\partial_s y = \sin\theta$. The unit vectors tangent and normal to the body are $\hat{\mathbf{s}} = (\partial_s x, \partial_s y)$ and $\hat{\mathbf{n}} = (-\partial_s y, \partial_s x)$, respectively. We write

$$\theta(s,t) = \theta_0(t) + \Delta\theta_1(t)H(s-1/3) + \Delta\theta_2(t)H(s-2/3), \tag{1}$$

where H is the Heaviside function and $\theta_0(t)$ is the tangent angle at the "tail" (the $s = 0$ end), an unknown to be solved for using Newton's equations of motion. The body position is obtained by integrating θ:

$$x(s,t) = x_0(t) + \int_0^s \cos\theta(s',t)ds', \tag{2}$$

$$y(s,t) = y_0(t) + \int_0^s \sin\theta(s',t)ds'. \tag{3}$$

The tail position $\mathbf{X}_0(t) = (x_0(t), y_0(t))$ and tangent angle $\theta_0(t)$ are determined by the force and torque balance for the body, i.e., Newton's second law [25,29]:

$$\int_0^L \rho\partial_{tt}x\,ds = \int_0^L f_x ds, \tag{4}$$

$$\int_0^L \rho\partial_{tt}y\,ds = \int_0^L f_y ds, \tag{5}$$

$$\int_0^L \rho\mathbf{X}^\perp\cdot\partial_{tt}\mathbf{X}\,ds = \int_0^L \mathbf{X}^\perp\cdot\mathbf{f}\,ds. \tag{6}$$

Here L is the body length, ρ is the body's mass per unit length, and $\mathbf{X}^\perp = (-y, x)$. For simplicity, the body is assumed to be locally inextensible, so L is constant in time. $\mathbf{f}$ is the force

per unit length on the body due to Coulomb friction with the ground:

$$\mathbf{f}(s,t) \equiv -\rho g \mu_n (\widehat{\partial_t \mathbf{X}_\delta} \cdot \hat{\mathbf{n}})\hat{\mathbf{n}} - \rho g (\mu_f H(\widehat{\partial_t \mathbf{X}_\delta} \cdot \hat{\mathbf{s}}) + \mu_b [1 - H(\widehat{\partial_t \mathbf{X}_\delta} \cdot \hat{\mathbf{s}})])(\widehat{\partial_t \mathbf{X}_\delta} \cdot \hat{\mathbf{s}})\hat{\mathbf{s}}, \tag{7}$$

$$\widehat{\partial_t \mathbf{X}_\delta} \equiv \frac{(\partial_t x, \partial_t y)}{\sqrt{\partial_t x^2 + \partial_t y^2 + \delta^2}}, \tag{8}$$

and g is gravitational acceleration. Again H is the Heaviside function, and $\widehat{\partial_t \mathbf{X}_\delta}$ is the normalized velocity, regularized with a small parameter $\delta = 10^{-3}$ here. Nonzero δ avoids nonsolvability of the equations in a small number of cases in which static friction comes into play, but δ has little effect on the solutions as long as it is much smaller than the scale of body velocities [typically $O(1)$], as detailed in [37] in the isotropic case. We find empirically that there is little change in the results (less than 1% in relative magnitude) when δ is decreased below 10^{-3}.

According to (7), the body experiences friction with different coefficients for motions in different directions with respect to the body. The frictional coefficients are μ_f, μ_b, and μ_n for motions in the forward ($\hat{\mathbf{s}}$), backward ($-\hat{\mathbf{s}}$), and normal ($\pm\hat{\mathbf{n}}$) directions, respectively. If $\mu_b \neq \mu_f$, we define the forward direction so that $\mu_f < \mu_b$, without loss of generality. In general, the body velocity at a given point has both tangential and normal components, and the frictional force density has components acting in each direction. A similar decomposition of force into directional components occurs for viscous fluid forces on slender bodies [40].

We assume that the body shape $(\Delta\theta_1(t), \Delta\theta_2(t))$ is periodic in time with period T, as is typical for steady locomotion [29]. We nondimensionalize Eqs. (4)–(6) by dividing lengths by the body length L, time by T, and mass by ρL. Dividing both sides by g, we obtain

$$\frac{L}{gT^2}\int_0^1 \partial_{tt} x \, ds = \int_0^1 f_x ds, \tag{9}$$

$$\frac{L}{gT^2}\int_0^1 \partial_{tt} y \, ds = \int_0^1 f_y ds, \tag{10}$$

$$\frac{L}{gT^2}\int_0^1 \mathbf{X}^\perp \cdot \partial_{tt}\mathbf{X} \, ds = \int_0^1 \mathbf{X}^\perp \cdot \mathbf{f} \, ds. \tag{11}$$

In (9)–(11) and from now on, all variables are dimensionless. If the body accelerations are not very large, as is often the case for robotic and real snakes [29], $L/gT^2 \ll 1$, which means that the body's inertia is negligible. By setting inertia—and the left-hand sides of (9)–(11)—to zero, we simplify the equations considerably:

$$\int_0^1 f_x ds = \int_0^1 f_y ds = \int_0^1 \mathbf{X}^\perp \cdot \mathbf{f} \, ds = 0. \tag{12}$$

Similar models were used in [15,21,25,28,29,41,42], and the same model was found to agree well with the motions of biological snakes in [29].

The distance traveled by the body's center of mass over one period is

$$d = \sqrt{\left(\int_0^1 x(s,1) - x(s,0) ds\right)^2 + \left(\int_0^1 y(s,1) - y(s,0) ds\right)^2}, \tag{13}$$

also equal to the time-averaged speed of the center of mass, $\|\overline{\partial_t \mathbf{X}}\|$, where the overbar denotes time and space (t and s) average. The work done by the body against friction over one period is

$$W = \int_0^1 \int_0^1 -\mathbf{f}(s,t) \cdot \partial_t \mathbf{X}(s,t) \, ds \, dt, \tag{14}$$

also equal to the time-averaged power expended against frictional forces, $\langle P \rangle$. As in previous works [15,21,25,29], we define the efficiency of locomotion as

$$\lambda = \frac{d}{W} = \frac{\|\overline{\partial_t \mathbf{X}}\|}{\langle P \rangle}. \tag{15}$$

Other definitions of efficiency that consider rotational motion (possibly useful for maneuverability) could also be considered. The upper bound on efficiency is

$$\lambda_{ub} = \frac{1}{\min(\mu_f, \mu_b, \mu_n)}, \tag{16}$$

corresponding to uniform motion in the direction of least friction, and it can be approached by a sequence of particular concertina-like motions, as shown in [37]. In this work, we take the relative efficiency λ/λ_{ub} as the primary measure of performance. For the case of zero body inertia considered here, we explained in [37] that d, W, λ, and the body motion depend only on the path traced by the kinematics in the $(\Delta\theta_1, \Delta\theta_2)$-plane, and not on how the path is parametrized by time. That is, if t is replaced by any nondecreasing function $\alpha(t)$ that maps the unit interval to itself, d, W, and λ are unchanged (in the limit $\delta \to 0$, and to a very good approximation for $\delta = 10^{-3}$).

III. SINGLE-HARMONIC (ELLIPTICAL) KINEMATICS

We begin by considering body kinematics given by a single harmonic, corresponding to elliptical trajectories in the $(\Delta\theta_1, \Delta\theta_2)$-plane:

$$\Delta\theta_1(t) = A_{10} + A_{11}\cos(2\pi t) + B_{11}\sin(2\pi t),$$
$$\Delta\theta_2(t) = A_{20} + A_{21}\cos(2\pi t) + B_{21}\sin(2\pi t), \quad 0 \leqslant t \leqslant 1. \tag{17}$$

An example is the gray ellipse in Fig. 3(a), with the coefficient values shown as vectors. For any path (17), the path is unchanged when t is shifted by an arbitrary constant phase. Although the path is unchanged, the net displacement of the body over a period, and hence the efficiency of the motion, depend on the phase if the body undergoes net rotation over a period.

As in previous works [3,24], we pay particular attention to the subset of paths that yield no net rotation of the body over one cycle, because these are the kinematics that yield nonzero net locomotion over a long-time average. If there

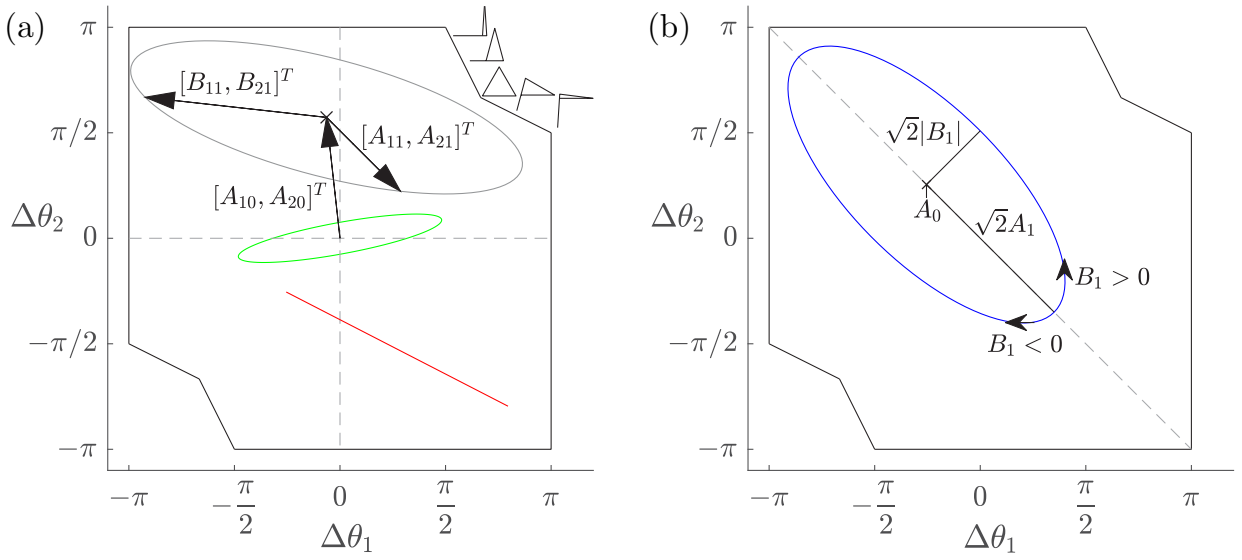

FIG. 3. (a) Examples of elliptical trajectories in the region of non-self-intersecting configurations (inside the black polygonal outline). Examples of body configurations at the boundary of the region are shown at the upper right. The gray ellipse has center A_{10}, A_{20} and shape given by $\{A_{11}, A_{21}, B_{11}, B_{21}\}$. (b) $(\Delta\theta_1(t), \Delta\theta_2(t))$ for a three-link body, symmetric about the line $\Delta\theta_1 = -\Delta\theta_2$. A_0 is the average of $\Delta\theta_1$ over the ellipse and $\sqrt{2}A_1$ and $\sqrt{2}|B_1|$ are the semimajor and semiminor axes of the ellipse. The sign of B_1 gives the direction in which the path is traversed.

is a nonzero net rotation, points on the body move along circles over large times, so the long-time average velocity is zero. However, such kinematics could still yield efficient locomotion over short-to-medium times, particularly if the net rotation is small. We consider this possibility later. In [37] we showed that no net rotation occurs for paths that have a certain bilateral symmetry, under reflection in the line $\Delta\theta_1 = -\Delta\theta_2$, e.g., the blue ellipse in panel (b). In that work, we discussed the case $\mu_b = \mu_f$, but the same argument holds if $\mu_b \neq \mu_f$. The rotation that occurs as the body traverses the half-ellipse above the line $\Delta\theta_1 = -\Delta\theta_2$ is canceled by the rotation that occurs on the half-ellipse below the line. Ellipses with bilateral symmetry can be parametrized as

$$\begin{aligned}\Delta\theta_1(t) &= A_0 + A_1\cos(2\pi t) + B_1\sin(2\pi t),\\ \Delta\theta_2(t) &= -A_0 - A_1\cos(2\pi t) + B_1\sin(2\pi t), \quad 0 \leqslant t \leqslant 1\end{aligned} \tag{18}$$

with only three parameters versus six (counting the phase) for general ellipses. We may take $A_1 \geqslant 0$ without loss of generality by shifting $t \to t + 1/2$ if necessary, which leaves the path unchanged. For motions with no net rotation, this change of phase does not change the displacement or efficiency.

Another set of paths that yield no net rotation are those with antipodal symmetry, i.e., symmetry with respect to reflection in the origin, such as the green ellipse in panel (a). At antipodal points, $\Delta\theta_1$ and $\Delta\theta_2$ are reversed in sign, and so are $\partial_t\Delta\theta_1$ and $\partial_t\Delta\theta_2$. Therefore, the shapes and kinematics of the body are mirror images when viewed in the body frame—defined here as the frame in which the tail lies at the origin, with zero tangent angle. Equations (12) are solved by equal and opposite values of $d\theta_0(t)/dt$ and mirror image vectors $d\mathbf{X}_0/dt$ in the body frame, because they result in mirror-image distributions of $\mathbf{f}$ in the body frame, which both satisfy Eqs. (12). Hence the body rotations at antipodal points cancel, and the net rotation over a full path is zero. Ellipses with antipodal symmetry are also parametrized by three parameters,

$$\begin{aligned}\Delta\theta_1(t) &= A_{11}\cos(2\pi t) + B_{11}\sin(2\pi t),\\ \Delta\theta_2(t) &= -A_{11}\cos(2\pi t) + B_{21}\sin(2\pi t), \quad 0 \leqslant t \leqslant 1,\end{aligned} \tag{19}$$

where A_{21} has again been set to $-A_{11}$ to fix the arbitrary phase.

The lack of net rotation for trajectories with bilateral and antipodal symmetry was also shown by [43]. A third special case that we discuss later is reciprocal kinematics—kinematics that are the same under time reversal. These are degenerate ellipses that reduce to straight line segments, e.g., the red line in panel (a). These yield no net locomotion if $\mu_b = \mu_f$, but they can yield efficient locomotion in other cases.

A. Efficient single-harmonic kinematics

We begin by studying the performance of trajectories given by ellipses with bilateral symmetry [e.g., Fig. 3(b)]. We consider (A_0, A_1, B_1) ranging over a three-dimensional grid in which A_0 and B_1 range from -1.2π to 1.2π, and A_1 from 0 to 1.2π, each in increments of $\pi/20$. Outside of these coefficient ranges, elliptical trajectories are generally not valid because they contain self-intersecting body shapes. We thus obtain a set that fills the space of kinematically valid ellipses somewhat densely. For the ellipses that lie entirely in the non-self-intersecting region (about 8000), we compute the body motions, work done against friction, and the relative efficiency λ/λ_{ub} using precomputed velocity maps, as described in [37]. We compute the results for the friction coefficient ratios $(\mu_n/\mu_f, \mu_b/\mu_f)$ ranging over a 12-by-8 grid with values ranging widely in magnitude, shown on the axes of Fig. 4(a). For each $(\mu_n/\mu_f, \mu_b/\mu_f)$ pair, we compute the top two local optima for efficiency, obtaining $12\times8\times2 = 192$ optima in

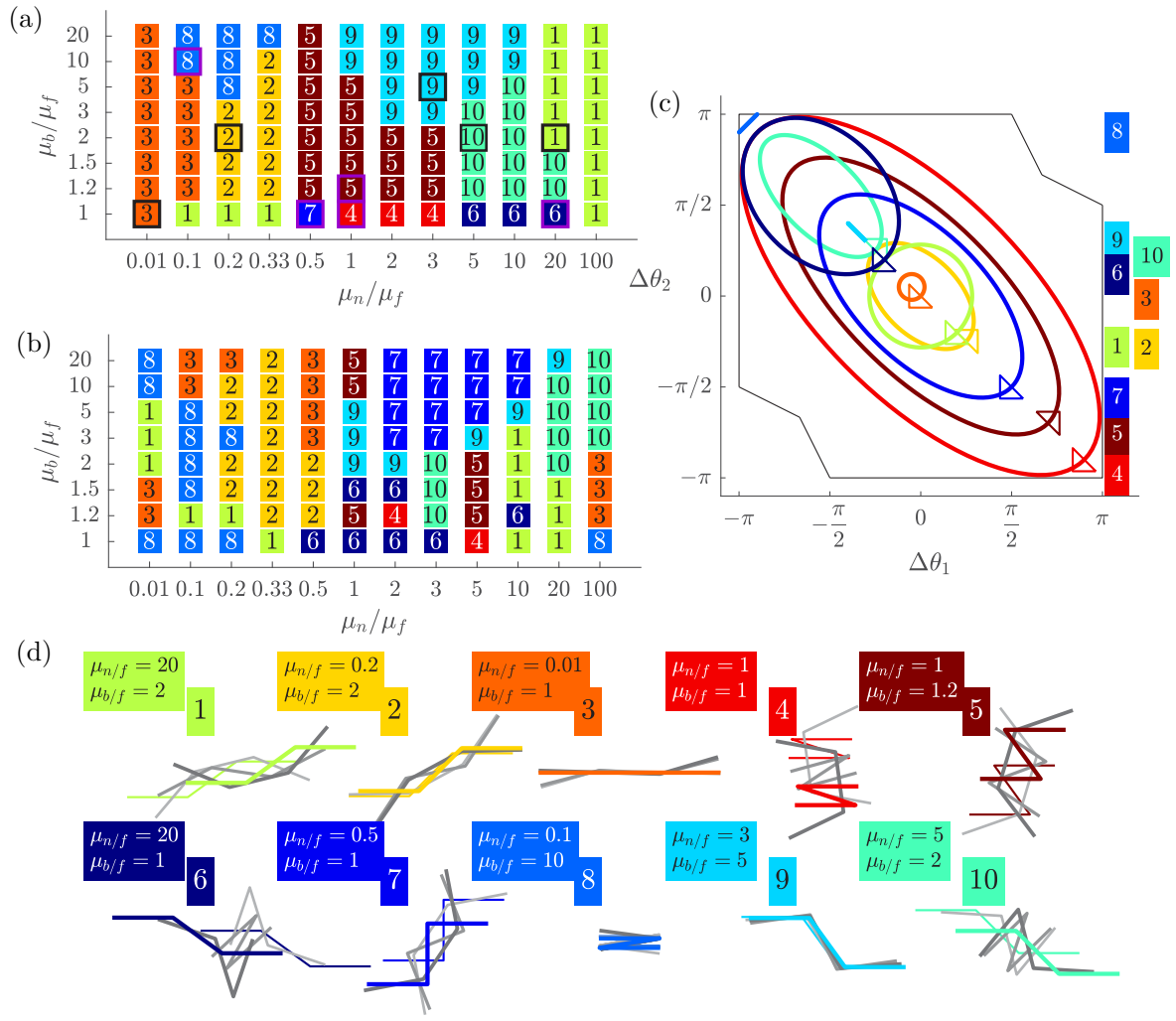

FIG. 4. Cluster classification of the best [panel (a)] and the second best [panel (b)] local optima in efficiency for elliptical trajectories across a grid of $(\mu_n/\mu_f, \mu_b/\mu_f)$ values. The set of 192 local optima are used to define 10 clusters based on proximity in (A_0, A_1, B_1) space. At each $(\mu_n/\mu_f, \mu_b/\mu_f)$ pair, the number and color of the square denotes the cluster to which it belongs. (c) The elliptical trajectory of the optimum closest to the centroid of each cluster, with color corresponding to that cluster. The cluster number of each ellipse is located along the right side of the panel, at the minimum vertical position of the corresponding ellipse. Each ellipse corresponds to a square in panel (a) that is outlined in black or purple. (d) For each ellipse in (c), snapshots of the body motion at five instants spaced 1/4 period apart, starting from the thin colored line, proceeding from light to dark gray, and ending with the thick colored line. The friction coefficient ratios for each motion are labeled, with the abbreviations $\mu_{n/f}$ and $\mu_{b/f}$ in place of μ_n/μ_f and μ_b/μ_f.

total. We then use a k-means clustering algorithm (specifically, the "kmeans" function in MATLAB) to partition the optima into 10 clusters based on location in (A_0, A_1, B_1)-space. With just 10 clusters, we reduce the number of optima to consider while approximating each of the 192 optima well by the nearest cluster centroid. In Fig. 4, the clusters corresponding to the best [panel (a)] and second best [panel (b)] optima are shown by numbered and colored squares at the corresponding $(\mu_n/\mu_f, \mu_b/\mu_f)$ pairs. Panel (c) shows trajectories for the optima closest to the centroid of each cluster, shown by outlined squares in panel (a). Panel (d) shows snapshots of the body motions corresponding to each of the 10 ellipses in panel (c). Each sequence of snapshots in panel (d) starts from the thin colored line, proceeds from light gray to dark gray, and ends with the thick colored line. An animation of these motions is shown in the supplemental material.

We see in panels (a) and (b) that each cluster (i.e., color) tends to occur in a few distinct regions of $(\mu_n/\mu_f, \mu_b/\mu_f)$ space. In other words, the friction coefficient ratios tend to select certain types of motions as optima. In Fig. 1 (from results in [21]), we sorted the optima for smooth bodies into three wavelike motions. It was difficult to obtain convergence to local optima at many $(\mu_n/\mu_f, \mu_b/\mu_f)$ values in the smooth case. Also, many of the optima in [21] were difficult to classify, and they did not correspond to the wavelike classification. With the smaller parameter space represented by elliptical trajectories of three-link bodies, here we are able to identify all local optima and sort them more precisely. Unlike the three wave-type categories, the 10 clusters here cover all of the kinematic parameter space [given by (A_0, A_1, and B_1)]. In panels (a) and (b), the 10 clusters overlap in multiple ways, but seven major regions in $(\mu_n/\mu_f, \mu_b/\mu_f)$-space can be identified as follows:

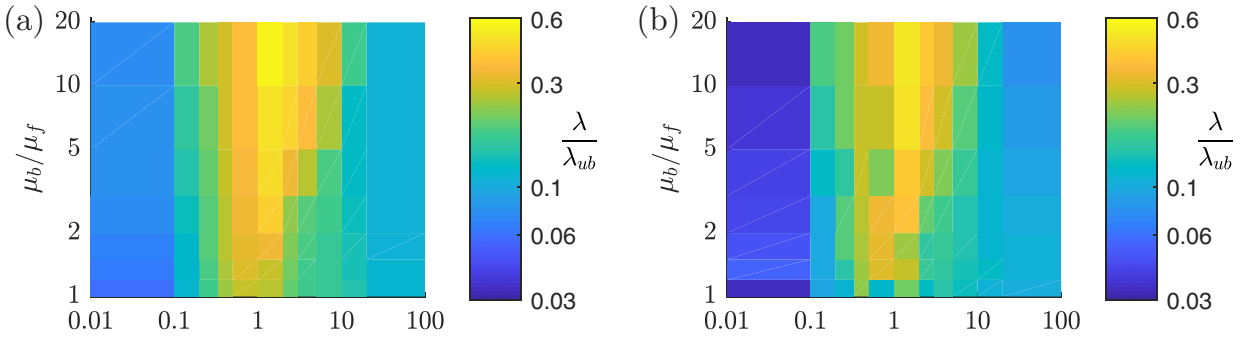

FIG. 5. Relative efficiencies of the global (a) and second-best optima (b) among elliptical trajectories with bilateral symmetry.

(i) $\mu_n/\mu_f \ll 1$, represented by optima 1, 3, and 8 [shown in panel (d)]. Optima 3 and 8 have very small amplitudes about motions that are nearly flat or completely folded, respectively, and move with a slight motion mainly in the normal direction when $\mu_n/\mu_f \ll 1$.

(ii) $0.1 < \mu_n/\mu_f < 1$, represented by optimum 2. This is a somewhat larger amplitude version of optimum 3, and it translates in both normal and tangential directions.

(iii) In the vicinity of isotropic friction, $\mu_n/\mu_f \approx 1$, $\mu_b/\mu_f \approx 1$ is a heterogeneous region in which two large-amplitude motions (4 and 6) predominate.

(iv) $\mu_n/\mu_f \approx 1$, $\mu_b/\mu_f > 1$. The brown optimum (5) is the most common here. It is a large-amplitude motion that translates roughly tangent to the body's mean flat state. This is a heterogeneous region with both small- and large-amplitude motions (3, 6, and 9).

(v) $\mu_n/\mu_f > 1$, $\mu_b/\mu_f > 1$, but not $\gg 1$. The optima are mainly 5 and 10, both large-amplitude motions.

(vi) $\mu_n/\mu_f > 1$, $\mu_b/\mu_f \gg 1$. Here the optima are mainly 7 (a large-amplitude motion) and 9 (a very small-amplitude motion).

(vii) $\mu_n/\mu_f \gg 1$. Here 1, 3, and 10 predominate, and the body moves mainly in the tangential direction. 10 roughly resembles the concertina motion of snakes, in which the front and rear of the body contract and expand alternately, while 1 resembles lateral undulation, i.e., a traveling wave along the body.

Like the smooth case, the three-link case shows a rough partition based on small, medium, and large values of μ_n/μ_f, with additional divisions based on μ_b/μ_f. It is interesting that at most $(\mu_n/\mu_f, \mu_b/\mu_f)$ values, the colors in panels (a) and (b) differ, so the top two optima come from different clusters. One might have expected the top two optima to be nearby motions within the same cluster. This is the case in most of the region where yellow squares are found, but it is rarely true elsewhere. This could result from a relatively smooth efficiency landscape in most cases, without large numbers of closely spaced optima. Six of the ten optimal paths in panel (c) are symmetric or nearly symmetric about the origin, meaning they oscillate about a flat mean shape. The remaining four (6, 8, 9, and 10) oscillate about mean shapes that are folded to a large extent. We also find that the undulatory optimum 1 is common both at $\mu_n/\mu_f \ll 1$ and $\gg 1$, but not at intermediate values (similar kinematics give zero net locomotion with isotropic friction [37]). The small-amplitude motions 3 and 8 also appear where μ_n/μ_f is very small and very large.

Figure 5 shows the relative efficiencies of the global [panel (a)] and second-best optima [panel (b)] in these regions. The corresponding A_0, A_1, and B_1 values are plotted in Fig. 15 of the Appendix. The maximum relative efficiency, nearly 0.6, is achieved at $\mu_n/\mu_f = 1$ and $\mu_b/\mu_f = 20$, the top center of panel (a), by kinematics in the cluster represented by motion 9 in Fig. 4(d)—a very small-amplitude reciprocal kinematics. The second best optimum at the same friction coefficient ratios [top center of panel (b)] is nearly as good, but it corresponds to a very different kinematics—number 5 in Fig. 4(d). The motion shown there is for an optimum at the same μ_n/μ_f but a much smaller μ_b/μ_f (1.2). The maximum relative efficiencies decline smoothly and monotonically in all directions moving away from the top center of panel (a). At the bottom center of panel (a) is isotropic friction, with maximum relative efficiency 0.26. The kinematics are given by the large red ellipse in Fig. 4(c), and the motion is number 4 in panel (d). Moving to the lower left corner of Fig. 5(a), $\mu_n/\mu_f = 0.01$ and $\mu_b/\mu_f = 1$, the relative efficiency drops to 0.06, its minimum over the panel, given by motion 3 in Fig. 4(d). Here, even a small amount of tangential motion causes a large drop in relative efficiency. At the other extreme, $\mu_n/\mu_f = 100$, the relative efficiency is 0.1, and it is achieved by a small-amplitude circular trajectory about the origin (the flat state), similar to the kinematics of motion 3 in Fig. 4(d), but now resulting in mainly *tangential* motion. For both $\mu_n/\mu_f \ll 1$ and $\gg 1$, the single harmonic and the three-link body do not permit sufficiently fine scale motions to come close to the upper bound of efficiency. We will see later that adding more harmonics allows a large improvement in efficiency for $\mu_n/\mu_f \ll 1$, but less so for $\mu_n/\mu_f \geqslant 1$, for three-link bodies.

The relative efficiencies of the second-best optima, shown in Fig. 5(b), are 70–99% of those of the best optima over most of the middle parts of the panels, but they drop to 30–60% of the best values at the most extreme values of μ_n/μ_f, 0.01 and 100. The values have a general pattern of decrease from a peak at the top center that is similar to panel (a), but with a bit less monotonicity. We discuss corresponding patterns in the variation of the coefficients $\{A_0, A_1, \text{and } B_1\}$ in the Appendix.

So far we have considered elliptical trajectories with bilateral symmetry, a three-parameter space. We now enlarge to

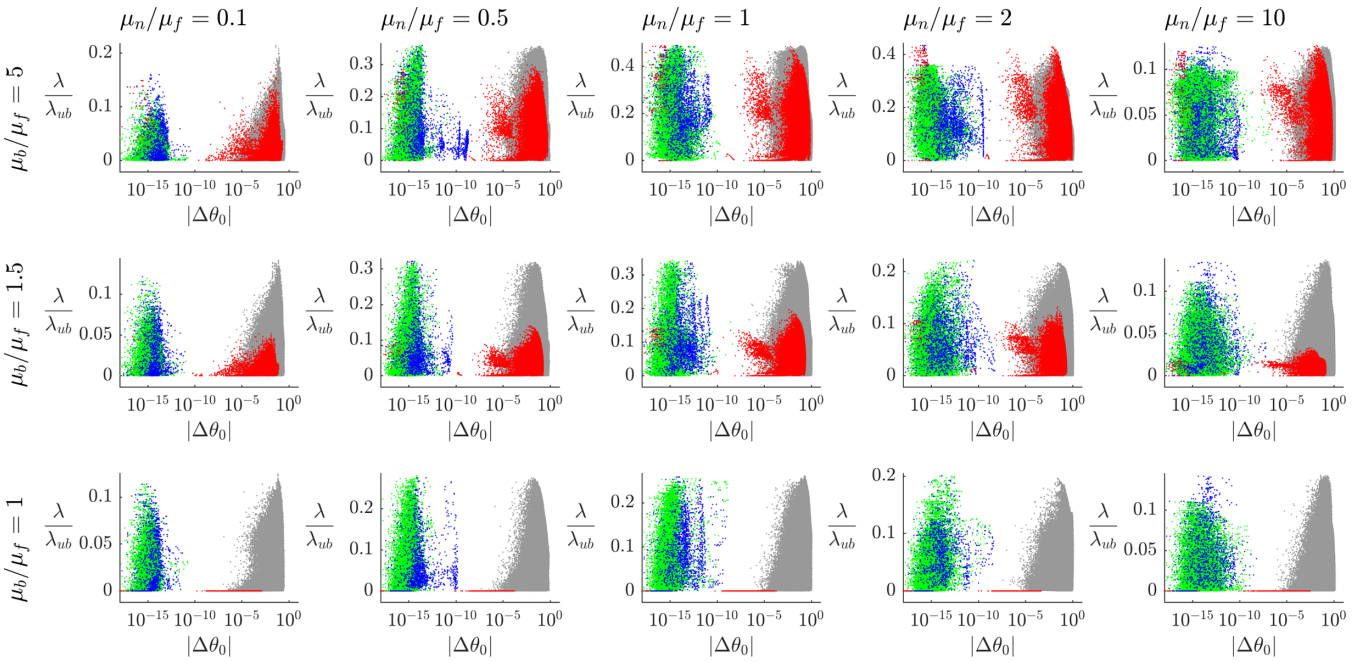

FIG. 6. Relative efficiency (λ/λ_{ub}) vs net rotation ($|\Delta\theta_0|$, in radians) for elliptical trajectories that are bilaterally symmetric (blue dots), antipodally symmetric (green dots), or reciprocal (red dots). Values for other trajectories are shown by gray dots. Each panel shows data at a given pair of friction coefficient ratios, labeled along the top and left of the figure.

the full six-parameter space of arbitrary elliptical trajectories, most of which have nonzero net rotations. We investigate to what extent efficient locomotion can occur with nonzero but small (possibly very small) net rotation. If some nonsymmetric motions have negligible rotation and greatly outperform the symmetric cases with zero net rotation (exemplified by the green and blue ellipses in Fig. 3), we should consider the larger space of nonsymmetric motions further. We consider the general ellipse in (17), first reducing to a five-dimensional space by fixing the phase (which does not change the path), and then varying the phase for each path. We fix the phase by taking $A_{21} = -A_{11}$ and $A_{11} \geqslant 0$. Each parameter in (17) varies from -1.2π to 1.2π (except A_{11}, varying from 0 to 1.2π) in increments of $\pi/20$. Restricting to paths in the region of non-self-intersecting bodies, we obtain 4.7×10^6 ellipses (compared to about 8000 in the bilaterally symmetric case), a large increase due to exponential growth with parameter space dimension. For each path, we vary the phase from 0 to 2π because the phase affects the displacement and hence the efficiency when there is nonzero net rotation. In Fig. 6, we plot the relative efficiency versus net rotation (in radians) for the general elliptical trajectories for various friction coefficient ratios. Each panel has a different set of friction coefficient ratios (labeled along the left and top of the figure), on a 5-by-3 grid that is a subset of the 12-by-8 grid considered earlier. Each trajectory is represented by a dot, gray for nonsymmetric, blue for bilaterally symmetric, green for antipodally symmetric, and red for reciprocal (as in the examples of Fig. 3).

The gray dots can have very small rotations, as small as 10^{-8} in some cases. However, the green and blue dots' rotations are generally orders of magnitude smaller, $\in [10^{-18}, 10^{-10}]$. These rotations are not precisely zero due to numerical roundoff error. In most panels, the green and blue dots achieve top efficiencies that are essentially the same as those of the much larger sets of gray dots. However, in the top two panels of the first column ($\mu_n/\mu_f = 0.1$), the gray dots reach efficiencies that are 20–30% higher. Excluding those with net rotations $>10^{-2}$ decreases this advantage substantially. Among the gray dots there is a decline in relative efficiency as net rotation tends to zero, and the gray dots with highest efficiencies usually have net rotations $\gtrsim 10^{-3}$. Some of the gray dots are only slight perturbations of symmetric cases, so we would expect similar efficiencies with small but nonzero net rotations. The red dots (reciprocal motions) achieve zero net locomotion, and hence zero relative efficiency, in the bottom row ($\mu_b = \mu_f$). They underperform the other groups in the middle row, but they are equal or close to the top performers in the top row, particularly the right side ($\mu_n/\mu_f \geqslant 1$). In the middle and top rows, most reciprocal motions have nonzero and sometimes large rotations. However, a small group of red dots can be seen (by zooming in), distinct from the blue and green dots, with very small rotations ($\leqslant 10^{-15}$), and with high efficiencies. These are nonsymmetric versions of motions 8 and 9 in Fig. 4. Because the green and blue dots achieve nearly the same peak relative efficiencies as the gray dots, and they are fewer in number by many orders of magnitude, we consider only these symmetric cases when we add higher harmonics. It rapidly becomes impractical to compute all periodic trajectories with coefficients on the aforementioned grids as the number of coefficients increases above five. Nonsymmetric paths with up to two harmonics are described by nine coefficients. Using the same coefficient grids as for the nonsymmetric ellipses (with a single harmonic), an estimate of the factor of increase in computing time for the nine-dimensional space relative to the five-dimensional space is $49^4 \approx 6\times10^6$. Many coefficients

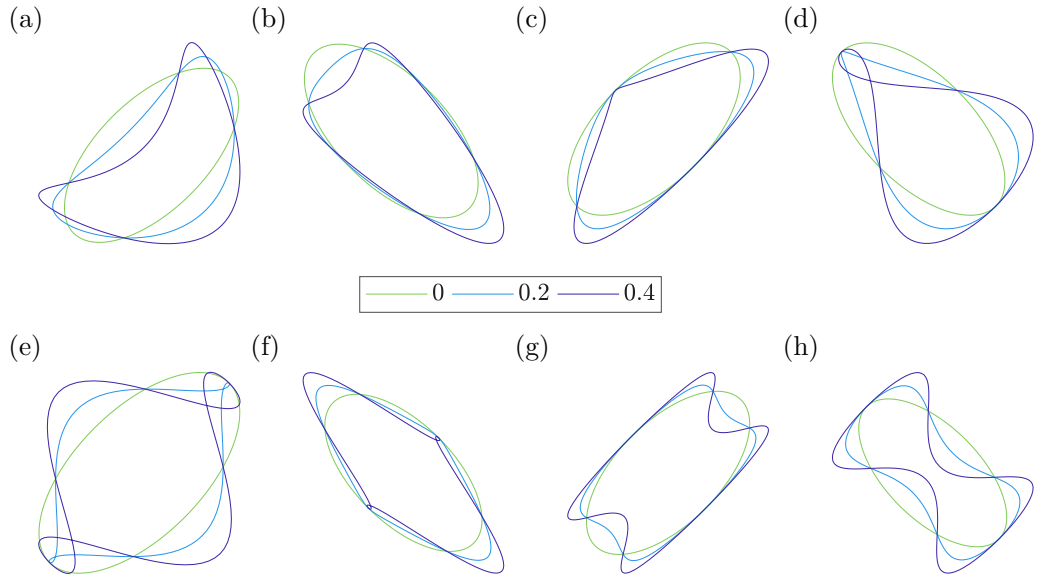

FIG. 7. Examples of the effect of adding higher harmonics to elliptical trajectories. The trajectories are given by (20). In (a), (c), (e), and (g), we have $A_1 = 0.5$ and $B_1 = 1$; in (b), (d), (g), and (h), we have $A_1 = 1$ and $B_1 = 0.5$. To these ellipses we add just one additional nonzero mode, setting either A_2 [in (a) and (b)], B_2 in [(c) and (d)], A_3 [(e) and (f)], or B_3 [(g) and (h)] to 0.2 (light blue lines) or 0.4 (dark blue lines).

lead to self-intersecting paths, but even after eliminating these, the factor of increase is many orders of magnitude and beyond our computing resources. Bilaterally symmetric trajectories with a given number of harmonics are described by half the coefficients of the nonsymmetric ones, allowing us to consider the full bilaterally symmetric trajectory parameter space with higher harmonics, but only a small number of them.

IV. MULTIPLE-HARMONIC KINEMATICS

We now add higher harmonics to elliptical trajectories, considering trajectories with bilateral symmetry here [e.g., the blue ellipse in Fig. 3(a)], and both bilateral and antipodal symmetry later. Trajectories with bilateral symmetry and harmonics up to k are given by

$$\begin{aligned}\Delta\theta_1(t) &= A_0 + \sum_{n=1}^{k} A_n \cos(2\pi nt) + B_n \sin(2\pi nt),\\ \Delta\theta_2(t) &= -A_0 + \sum_{n=1}^{k} -A_n \cos(2\pi nt) + B_n \sin(2\pi nt),\\ &\quad 0 \leqslant t \leqslant 1,\end{aligned} \tag{20}$$

while those with antipodal symmetry are given by

$$\begin{aligned}\Delta\theta_1(t) &= \sum_{\substack{n=1\\ n\,\text{odd}}}^{k} A_{1n} \cos(2\pi nt) + B_{1n} \sin(2\pi nt),\\ \Delta\theta_2(t) &= \sum_{\substack{n=1\\ n\,\text{odd}}}^{k} A_{2n} \cos(2\pi nt) + B_{2n} \sin(2\pi nt), \quad 0 \leqslant t \leqslant 1.\end{aligned} \tag{21}$$

In both cases we have $2k + 1$ terms [when we use $A_{21} = -A_{11}$ to set the arbitrary phase in (21)] compared to $4k + 2$ terms in the general nonsymmetric case, for $k \geqslant 1$. Figure 7 shows examples of bilaterally symmetric trajectories obtained by adding the second or third harmonics to the basic ellipse. In both rows, we start with example ellipses shown in green. These have just the A_1 and B_1 terms in (20), with all other terms zero. We take the major axis twice as long as the minor axis in these examples, so in (a), (c), (e), and (g) we have $A_1 = 0.5$ and $B_1 = 1$, while in (b), (d), (f), and (h) we have the other symmetric orientation, given by $A_1 = 1$ and $B_1 = 0.5$. To these ellipses we add just one additional nonzero mode, setting either A_2 [in (a) and (b)], B_2 [in (c) and (d)], A_3 [(e) and (f)], or B_3 [(g) and (h)] to 0.2 (light blue lines) or 0.4 (dark blue lines), and the other coefficients to zero. These examples show that the effects of the $4\pi t$ modes (top row) are approximately to dilate the path on one side and contract on the other, though the change of shape is nonuniform and somewhat complicated. The $6\pi t$ modes (bottom row) approximately dilate the path at one pair of opposite sides and contract at the other pair. The trajectories self-intersect in several cases [which is separate from the question of whether the body self-intersects, determined by the location of the trajectory in $(\Delta\theta_1, \Delta\theta_2)$-space]. Another, geometric interpretation of the terms in (20) and (21) was given by [44]: those with the lowest harmonic (1) represent an ellipse; those with harmonic 2 (i.e., with coefficients A_2 and B_2) also represent an ellipse, but one that is traversed twice within the unit period, and likewise for any harmonic n. Thus (20) and (21) can be thought of as superpositions of ellipses that are traversed integer numbers of times within the unit period.

It is very expensive to solve for the body motions for trajectories of the form (20) with $k > 2$ with a dense grid of coefficients, i.e., varying all $2k + 1$ coefficients on the aforementioned grids with spacing $\pi/20$. Instead, we consider two five-dimensional subspaces, the first consisting of ellipses

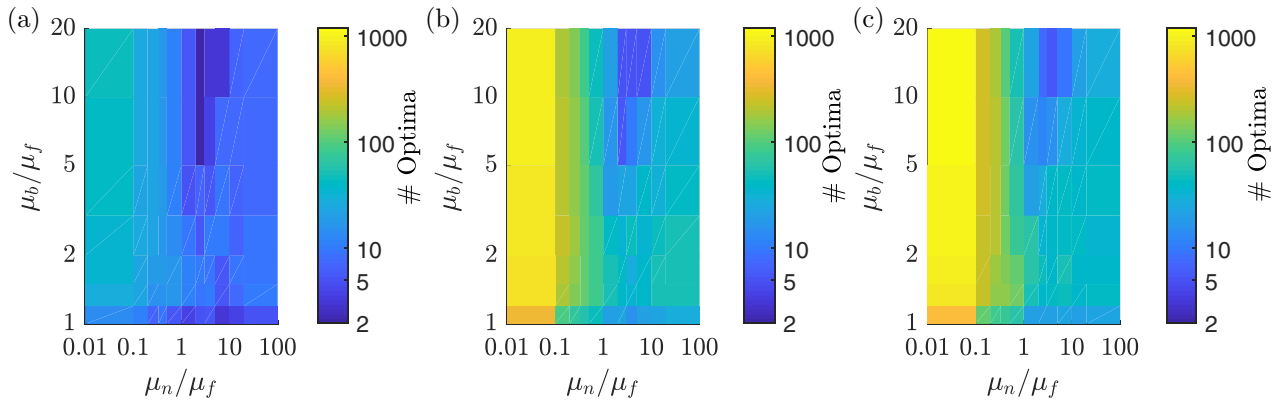

FIG. 8. The numbers of local optima of efficiency at various friction coefficient ratios in the space of $\{A_0, A_1, B_1\}$ describing bilaterally symmetric ellipses [panel (a)], the larger space of $\{A_0, A_1, B_1, A_2, B_2\}$ with second harmonics added [panel (b)], and the space of $\{A_0, A_1, B_1, A_3, B_3\}$ with third harmonics added [panel (c)].

plus second harmonics, varying $\{A_0, A_1, B_1, A_2, B_2\}$ on the aforementioned grids, and the second consisting of ellipses plus third harmonics, i.e., varying $\{A_0, A_1, B_1, A_3, B_3\}$ on the same grids. In Fig. 8 we plot the numbers of local optima for efficiency at various friction coefficient ratios. This quantity gives a measure of the smoothness of efficiency space. The number of optima for bilaterally symmetric ellipses, i.e., the space of $\{A_0, A_1, B_1\}$, is shown in panel (a); ellipses plus second harmonics are shown in panel (b); and ellipses plus third harmonics are shown in panel (c). In panel (a), the number of local optima has a minimum of two at the top, right of center, and a maximum of 45 at the top left. These are also locations where the relative efficiency was large and small for the best elliptical trajectories, according to Fig. 15(a). On the right side of Fig. 8(a) ($\mu_n/\mu_f > 1$), there are at most 10 optima, and about 2–4 times as many at points with the reciprocal value of μ_n/μ_f, on the left side. In panels (b) and (c), the numbers of local optima increase enormously at the top left to about 1000 in each case, while the minimum value of 2 in (a) increases modestly, to 4 and 6 in (b) and (c), respectively. At other points, the numbers of optima increase by factors of 4–8 typically, moving from (a) to (b) or to (c). The numbers of local optima plotted in Fig. 8 are found by comparing each value of efficiency on the mesh with those of its nearest neighbors [numbering 3^3-1 in panel (a), and 3^5-1 in panels (b) and (c)]. The numbers of optima presented in Fig. 8 are mesh-dependent, and they increase as the meshes are refined. When we decrease the mesh spacing from $\pi/20$ to $\pi/40$, the numbers of optima increase, with the largest increases where the numbers are highest in Fig. 8. At the smallest values ($\lesssim$10) there is little or no change. It is not computationally tractable to perform the computation on a mesh that is fine enough to fully resolve all the optima in these spaces, but the qualitative trends shown by Fig. 8 become stronger as the mesh is refined, and they are expected to persist in the continuum limit.

One might expect that the cases with larger numbers of local optima, and larger changes in the numbers of local optima when the higher harmonics are added, are more sensitive to small changes in body motions. One question is whether the optimal efficiencies in these cases [e.g., the values on the left side of Fig. 5(a)] have larger increases when higher harmonics are added.

Figure 9 shows the changes in peak efficiency when the parameter space is enlarged from smaller to larger sets of harmonics in (20). First, we consider the improvement when

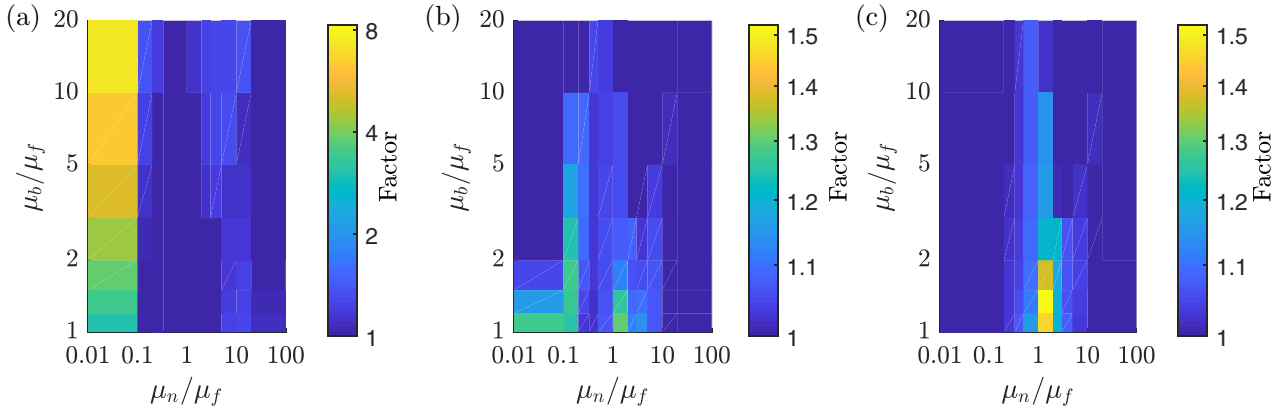

FIG. 9. The factor of improvement in maximum relative efficiency when the space of modes is enlarged from (a) $\{A_1, B_1\}$ to $\{A_0, A_1, B_1\}$; (b) $\{A_0, A_1, B_1\}$ to $\{A_0, A_1, B_1, A_2, B_2\}$; (c) $\{A_0, A_1, B_1\}$ to $\{A_0, A_1, B_1, A_3, B_3\}$. The modes corresponding to these coefficients are listed in Eqs. (20). The factor is plotted at various friction coefficient values shown on the axes.

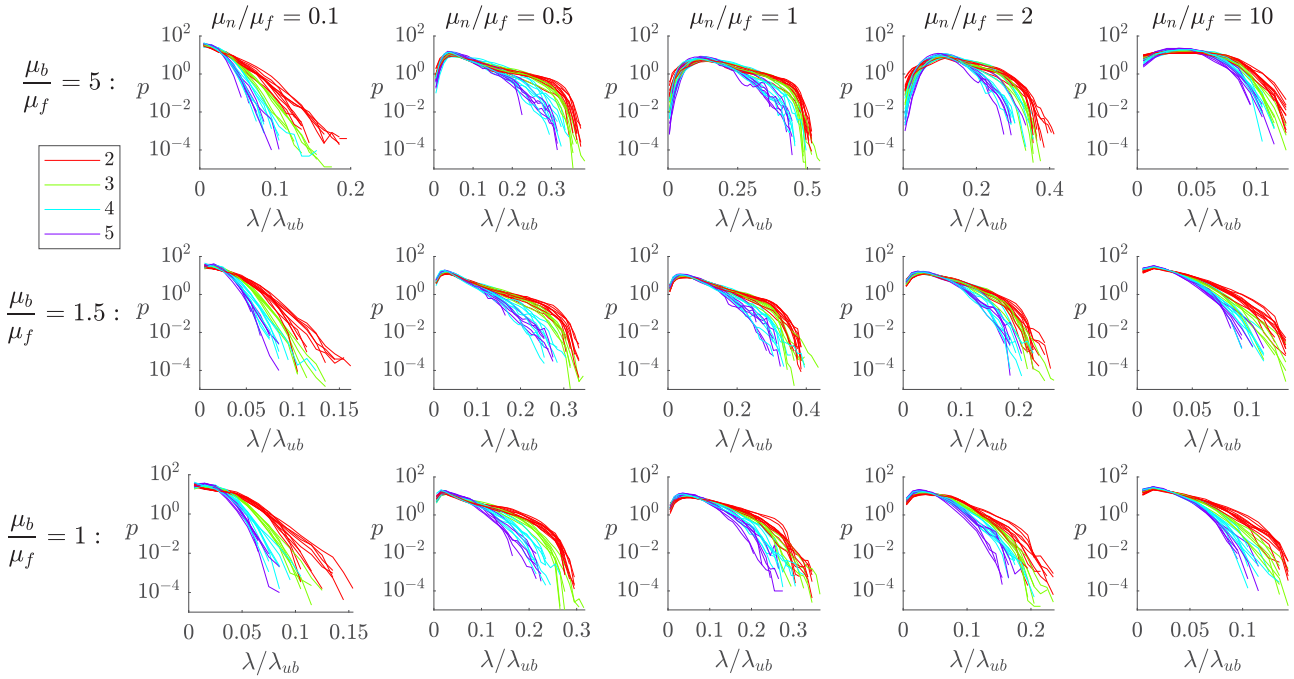

FIG. 10. Probability densities of relative efficiency, estimated from histogram data for various friction coefficient ratios (labeled at top and left). Each color corresponds to bilaterally symmetric trajectories with a given maximum harmonic k, labeled at left, resulting in $2k + 1$ modes. Each curve corresponds to a different random ensemble of about 10^6 trajectories.

motions that are biased with respect to the flat state (i.e., those with nonzero A_0) are considered, for elliptical trajectories. Panel (a) shows the factor of improvement in the peak efficiency when modes with $\{A_0, A_1, B_1\}$ are considered compared to those with just $\{A_1, B_1\}$. At the smallest μ_n/μ_f, the A_0 term allows for a large increase in the peak relative efficiency. At most other friction coefficient ratios, there is no improvement, except in a strip of values contained within $1 \leqslant \mu_n/\mu_f \leqslant 10$, where the improvement is typically 20–30 %. Panel (b) shows the improvement obtained by expanding from $\{A_0, A_1, B_1\}$ to $\{A_0, A_1, B_1, A_2, B_2\}$. It is somewhat surprising that in most cases here, there is little improvement from considering these two additional modes. There is little to no improvement except near isotropic friction and near $0.01 \leqslant \mu_n/\mu_f \leqslant 0.1$, where the improvement is at most 31%. Panel (c) shows the improvement from expanding from $\{A_0, A_1, B_1\}$ to $\{A_0, A_1, B_1, A_3, B_3\}$. Here too, the improvement is modest, with improvements up to 51% near isotropic friction, but less than 7.5% outside of $1/3 \leqslant \mu_n/\mu_f \leqslant 3$. Taken together, these results suggest that in most cases ellipses, in particular ellipses centered at the origin, may be good approximations to the optimal trajectories with large numbers of harmonics. Our stochastic optimization results shown later will support this statement, except in some cases with $\mu_n/\mu_f \ll 1$.

As the number of modes increases above five, it becomes prohibitively expensive to compute results across a grid that resolves all of the coefficient parameter space. We explore higher-dimensional spaces by instead selecting a random ensemble of $\approx 10^6$ points in coefficient space. For example, with harmonics up to $k = 3$, there are seven coefficients in (20). A large ensemble of seven-component vectors is chosen, with each of the seven components (the coefficients) drawn from a uniform distribution on $[-1.2\pi, 1.2\pi]$. Most points yield trajectories that include self-intersecting bodies at certain times, and these are eliminated. The relative efficiency is computed for the non-self-intersecting cases, $\approx 10^6$ in number. This is done for $k = 2$, 3, 4, and 5 harmonics, with coefficients in a $(2k + 1)$-dimensional space, and 10 different random ensembles in each case. For each ensemble, we bin the data in small increments of relative efficiency, and we construct an estimate of the probability density of relative efficiency, plotted for each k in Fig. 10, on the five-by-three grid of friction coefficient ratios used in Fig. 6. The maximum efficiencies (approximately the maximum of the values labeled on the horizontal axis in each panel) vary widely among the panels, but the density distribution shapes have certain common features. The densities typically have a peak at an efficiency that is some distance from zero (except in the leftmost column), the typical efficiency magnitude for a random kinematics. After the peak, the densities fall off exponentially (a linear behavior on this log-linear scale) or faster. They are many orders of magnitude smaller near the maximum efficiencies, which are therefore rare events. There is some scatter among the 10 different random ensembles (the set of 10 curves with the same color in each panel), particularly at the largest efficiencies. Nonetheless, the curves of a given color tend to cluster together, and near the peaks the densities are not very sensitive to the particular ensemble used. In most cases, $k = 2$ gives the best performance—the highest density of states at the largest efficiencies—and the performance decreases with larger k. The spaces with lower k are nested in those at higher k, so the maximum efficiency over all kinematics must occur in the space with largest k. However, Fig. 10 shows that it is unlikely to arise in the samples chosen. The method of sampling (uniform sampling in each coefficient, with self-intersecting motions discarded) could affect

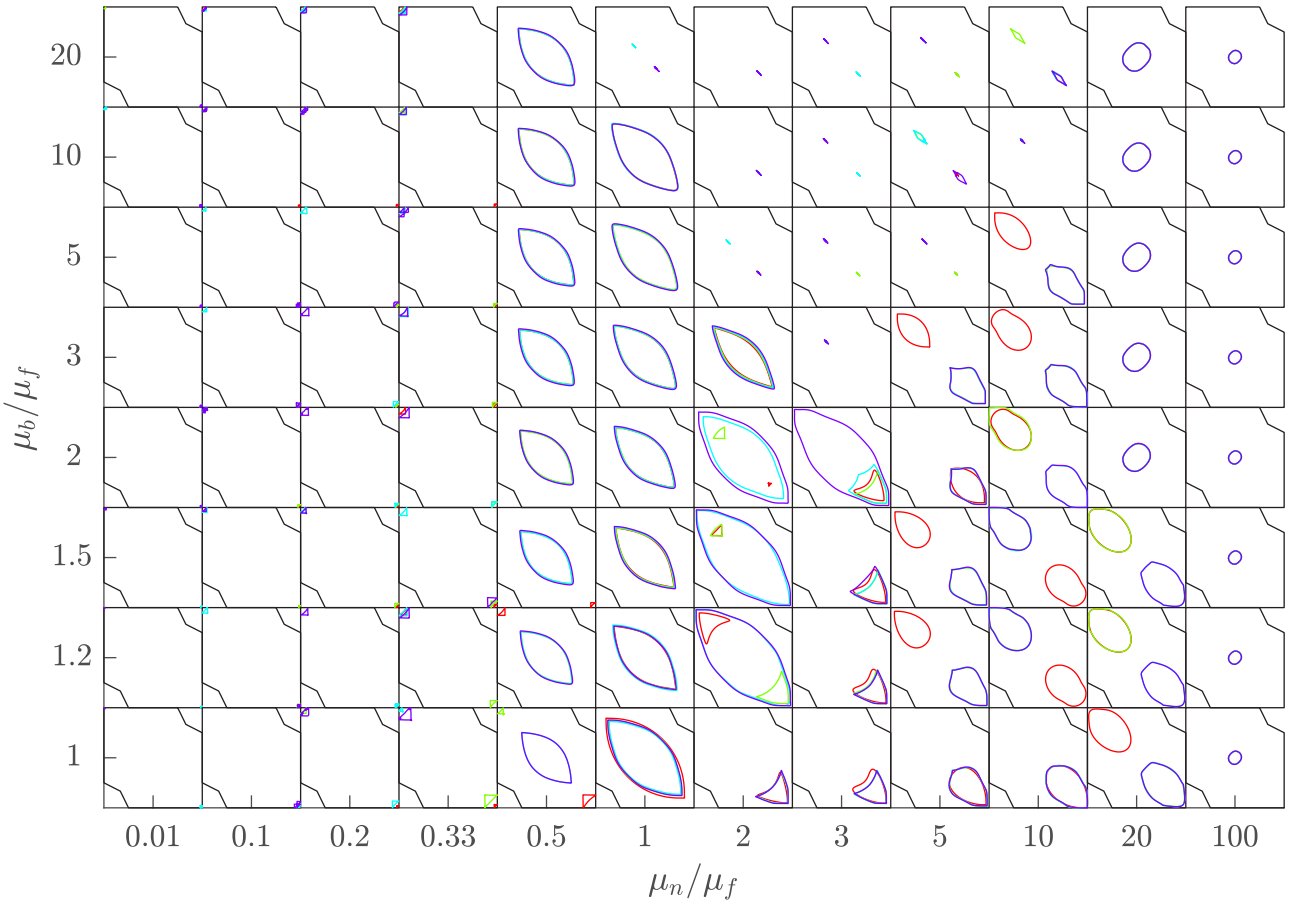

FIG. 11. Efficiency-maximizing trajectories with bilateral symmetry, with different maximum harmonics k—3 (red), 5 (green), 7 (light blue), and 9 (purple)—corresponding to $2k+1$ modes in each case. The trajectories are plotted in the region of nonintersecting trajectories, plotted at various friction coefficient ratios labeled at the bottom and left. The trajectories are computed with the stochastic optimization algorithm described in the text.

the increased prevalence of lower-efficiency states at larger k. For example, many kinematics with large high-harmonic components may be ineffective for locomotion, and these are likely to occur with the uniform sampling of each coefficient used here.

V. STOCHASTIC OPTIMIZATION

We have presented the relative efficiency for individual optima, their kinematics in the elliptical case, and some of the features of trajectory spaces—numbers of optima, distributions of rotations and efficiencies, and incremental improvements from enlarging the spaces of modes—with dimensions up to 11 (i.e., k up to 5). We now study the features of optimal trajectories as the space of modes is increased further by using a stochastic optimization method with ensembles of trajectories. Compared to the quasi-Newton approaches used in [3,21], the stochastic method is gradient-free, and therefore simpler to implement—particularly given the constraint that trajectories remain in the non-self-intersecting region. The main drawbacks are that more iterations are needed to obtain convergence, and the stochastic algorithm requires parameters that are tuned heuristically, unlike the more standardized Newton-type search algorithms [45].

Here we create a large number of populations (e.g., 250), each population with 50 trajectories, and we evolve the populations over many generations. At each generation, we evaluate the relative efficiency of each trajectory, select the top 50% of trajectories, and replace the entire population with random perturbations of the top 50%. We add perturbations to the coefficients, drawn from uniform or Gaussian distributions. The magnitude of each coefficient in a given perturbation is a tuned parameter, typically 0.001–0.01 multiplied by the reciprocal of the harmonic corresponding to the coefficient. If the perturbation magnitude is at the smaller end of the range, the population converges slowly but directly to the nearest local optimum. If the perturbation magnitude is at the larger end, the population converges more quickly and possibly to a wider range of optima, but it fluctuates more around a given optimum. Therefore, we start with a larger perturbation magnitude and progressively decrease it, as in simulated annealing [45]. We run each population for 1000 generations, by which point convergence is obtained.

In Fig. 11 we plot the optimal trajectories thus obtained, among all the populations, in friction coefficient space. The trajectories are plotted within the region of non-self-intersecting shapes, outlined in black at each pair of friction coefficient ratios. We consider trajectories with bilateral

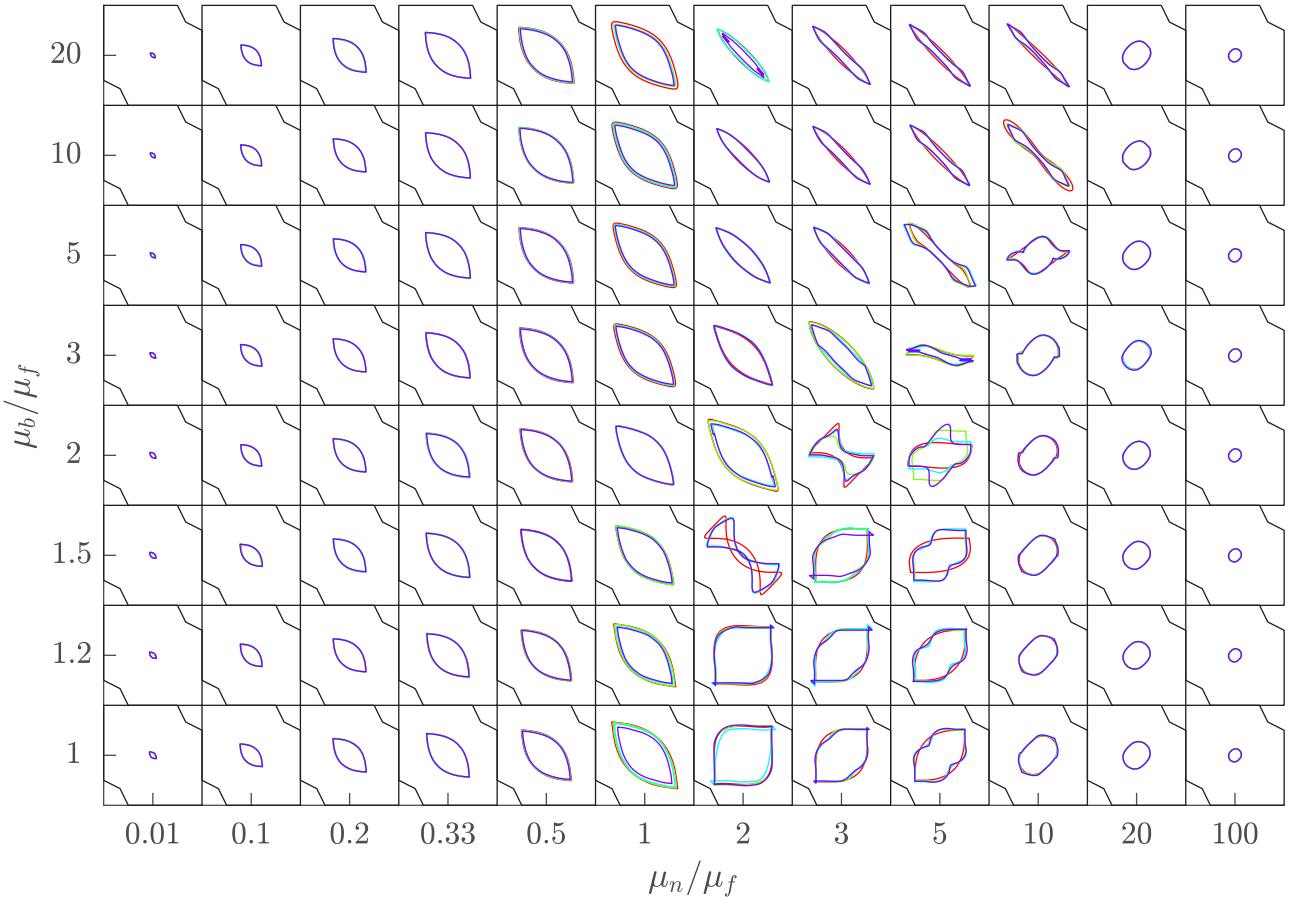

FIG. 12. Efficiency-maximizing trajectories with antipodal symmetry, with different maximum harmonics k—3 (red), 5 (green), 7 (light blue), and 9 (purple)—corresponding to $2k+2$ modes in each case. The trajectories are plotted in the region of nonintersecting trajectories, plotted at various friction coefficient ratios labeled at the bottom and left. The trajectories are computed with the stochastic optimization algorithm described in the text.

symmetry here. Different colors correspond to different maximum harmonics k in (20)—3 (red), 5 (green), 7 (light blue), and 9 (purple)—with $2k+1$ modes in each case. As for the elliptical trajectory optima in Fig. 4, certain types of trajectories are strongly correlated with certain regions of friction coefficient space. There is generally very good agreement between the optima with different k. On the left, $\mu_n/\mu_f \ll 1$, the optimal trajectories are very small, in most cases almost 45-45-90 right triangles with two sides aligned with the $\Delta\theta_1$ and $\Delta\theta_2$ axes, and close to the upper left or lower right corners of each subregion. These are two versions of the same motion (symmetric about the line $\Delta\theta_1 = \Delta\theta_2$, i.e., with $\Delta\theta_1$ and $\Delta\theta_2$ interchanged), with the body executing very small motions about a mean shape that is nearly completely folded together as in motion 8 of Fig. 4(d). The triangles are largest and easiest to see at $\mu_n/\mu_f = 0.33$ and $\mu_b/\mu_f = 1$, and gradually become smaller moving leftward and upward in friction coefficient space. There is a transition to much larger lenticular or oval-shaped trajectories, centered at the origin at $\mu_n/\mu_f = 0.5$. These become larger, eventually filling the non-self-intersecting region at $\mu_n/\mu_f = 2$ for some μ_b/μ_f. Here and at $\mu_n/\mu_f = 3$, triangular trajectories in the corners reappear, this time more curved and larger than previously. For larger μ_b/μ_f and $1 \leqslant \mu_n/\mu_f \leqslant 10$, small slit trajectories appear, very similar to motion 9 in Fig. 4(d), and occurring at similar friction coefficient values. At smaller μ_b/μ_f, as μ_n/μ_f ranges from 5 to 20, the corner trajectories become larger and rounder, and at the largest $\mu_n/\mu_f = 100$, all the trajectories become small circles at the origin, like kinematics 3 in Fig. 4(d), but symmetric about the flat state, and moving mainly tangentially at this pair of friction coefficient ratios. Most of these trajectories are simple closed curves that can be approximated reasonably well by ellipses.

Figure 12 shows the results with the same optimization procedure but for the other main class of zero-net-rotation trajectories—those with antipodal symmetry. The values of k are the same, but they result in $2k+2$ modes now using (21). Except in a few cases [e.g., (5,3),(10,5)], these trajectories also have the bilateral symmetry of the previous trajectories. Where the trajectories in Fig. 11 are centered at the origin, the two types of optima agree well. Where they disagree, if the antipodally symmetric optima also have bilateral symmetry (as in nearly every case), they must be inferior, or else they would also occur in Fig. 11. In general, the antipodally symmetric optima vary more smoothly in parameter space.

For all friction coefficient ratios, we find that the optima with bilateral symmetry are at least as good as those with antipodal symmetry, and often much better. The factors by

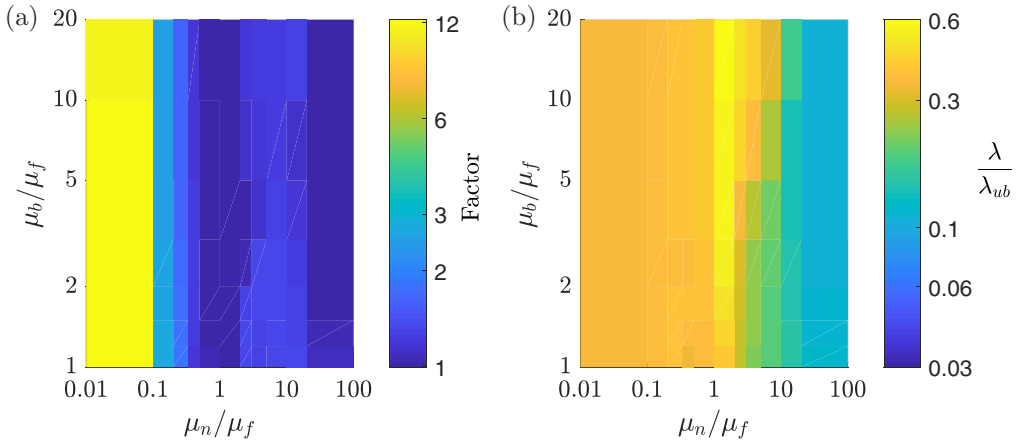

FIG. 13. (a) The factors by which the efficiencies of the bilaterally symmetric optima exceed those of the antipodally symmetric optima. (b) The relative efficiencies of the bilaterally symmetric optima.

which the efficiencies of the bilaterally symmetric optima exceed those of the antipodally symmetric optima are plotted in Fig. 13(a). The factor is about 12 at $\mu_n/\mu_f = 0.01$, 2.4–2.7 at $\mu_n/\mu_f = 0.1$, and decreases to about 1 at $\mu_n/\mu_f = 0.5$ and 1. It then rises again to 1.2–1.3 for $2 \leqslant \mu_n/\mu_f \leqslant 10$, and then drops back to 1 for larger μ_n/μ_f. The values of the relative efficiency for the bilaterally symmetric optima are shown in panel (b). They are fairly uniform, 0.34–0.42, on the left side of the panel, $0.01 \leqslant \mu_n/\mu_f \leqslant 0.5$. On the right side of the panel, they are similar to the values for the elliptical optima in Fig. 5(a), except near isotropic friction. There the bilaterally symmetric optima are about 60% more efficient, but the advantage decreases rapidly moving to larger μ_b/μ_f and μ_n/μ_f. This is consistent with the fact that the trajectories in Fig. 11 become either more rounded (at large μ_n/μ_f) or flat (at large μ_b/μ_f), in both cases closer to ellipses. For $\mu_n/\mu_f = 0.01$, the bilaterally symmetric optima are about six times as efficient as the elliptical optima. Here the efficiency is sensitive to the detailed shape of the trajectory (i.e., triangular versus flat), and the higher harmonics are needed to approximate the optimal trajectory for a three-link body.

A. Linear resistance

Many previous works have considered the optimal motions of three-link swimmers at zero Reynolds number [1–13]. To compare with this important case, we now consider how the optimal trajectories change when the resistive force is linear in velocity, instead of speed-independent as in the preceding results. This corresponds to resistive force theory, which is the lowest-order approximation to the nonlocal viscous forces on a slender body [40]. Although nonlocal slender body theories have also been developed and used extensively [3,30], resistive force theory gives a sufficient representation of the physics for many swimming problems [46–50]. The anisotropy ratio for a long cylinder, $\mu_n/\mu_f = 2$, has been used most often for a body swimming in a Newtonian fluid [2,30,40]. Reference [51] mentions a value of 1.5 as more appropriate for undulating bodies; Ref. [52] mentions values between 1 and 2 in an empirical theory for shear-thinning fluids; and Ref. [53] derives ratios both less than and greater than 2 for complex fluids. Ratios greater than 2 (of the order of 10) have also been used to model the crawling of micro-organisms on wet surfaces [48,54–56]. We are unaware of studies that derive ratios smaller than 1 for biological or physical swimmers, although Refs. [17,51] mention the possibility for the marine worm Nereis, which has enhanced resistance along the body axis due to bristles, and which uses direct wave locomotion. We are also unaware of swimmers that have been modeled with μ_b/μ_f different from 1, but some difference would occur with bodies that are not fore-aft symmetric. For comparison with the sliding locomotion results in this paper, we compute optimally efficient trajectories with the linear resistance law in the same space of ratios of resistance (previously friction) coefficients.

For the case of linear resistance, we replace $\widehat{\partial_t \mathbf{X}}_\delta$ by $\partial_t \mathbf{X}$ in (7). Bilaterally and antipodally symmetric trajectories still yield no net rotation; the cancellations in rotation are not affected by how the resistive force depends on the velocity magnitude. The definition of efficiency is changed from (15) to $\lambda = \|\overline{\partial_t \mathbf{X}}\|^2/\langle P\rangle$, and it is proportional to measures of efficiency (e.g., the "Lighthill efficiency") used in previous studies [2,3,57]. The same upper bound, $\lambda_{ub} = 1/\mu_{\min}$, holds with resistance that is linear in velocity, as follows. We now have

$$\langle P\rangle = \int_0^1\int_0^1 \mu_n(\partial_t\mathbf{X}\cdot\hat{\mathbf{n}})^2 + \{\mu_f H(\partial_t\mathbf{X}\cdot\hat{\mathbf{s}}) + \mu_b[1-H(\partial_t\mathbf{X}\cdot\hat{\mathbf{s}})]\}(\partial_t\mathbf{X}\cdot\hat{\mathbf{s}})^2 ds\,dt \geqslant \mu_{\min}\int_0^1\int_0^1 \|\partial_t\mathbf{X}\|^2 ds\,dt. \tag{22}$$

We decompose $\partial_t\mathbf{X}$ into its time-and-space average $\overline{\partial_t\mathbf{X}}$ plus the remainder $\widetilde{\partial_t\mathbf{X}}$, which has zero time-and-space average:

$$\partial_t\mathbf{X} = \overline{\partial_t\mathbf{X}} + \widetilde{\partial_t\mathbf{X}}, \quad \overline{\partial_t\mathbf{X}} \equiv \int_0^1\int_0^1 \partial_t\mathbf{X}\,ds\,dt. \tag{23}$$

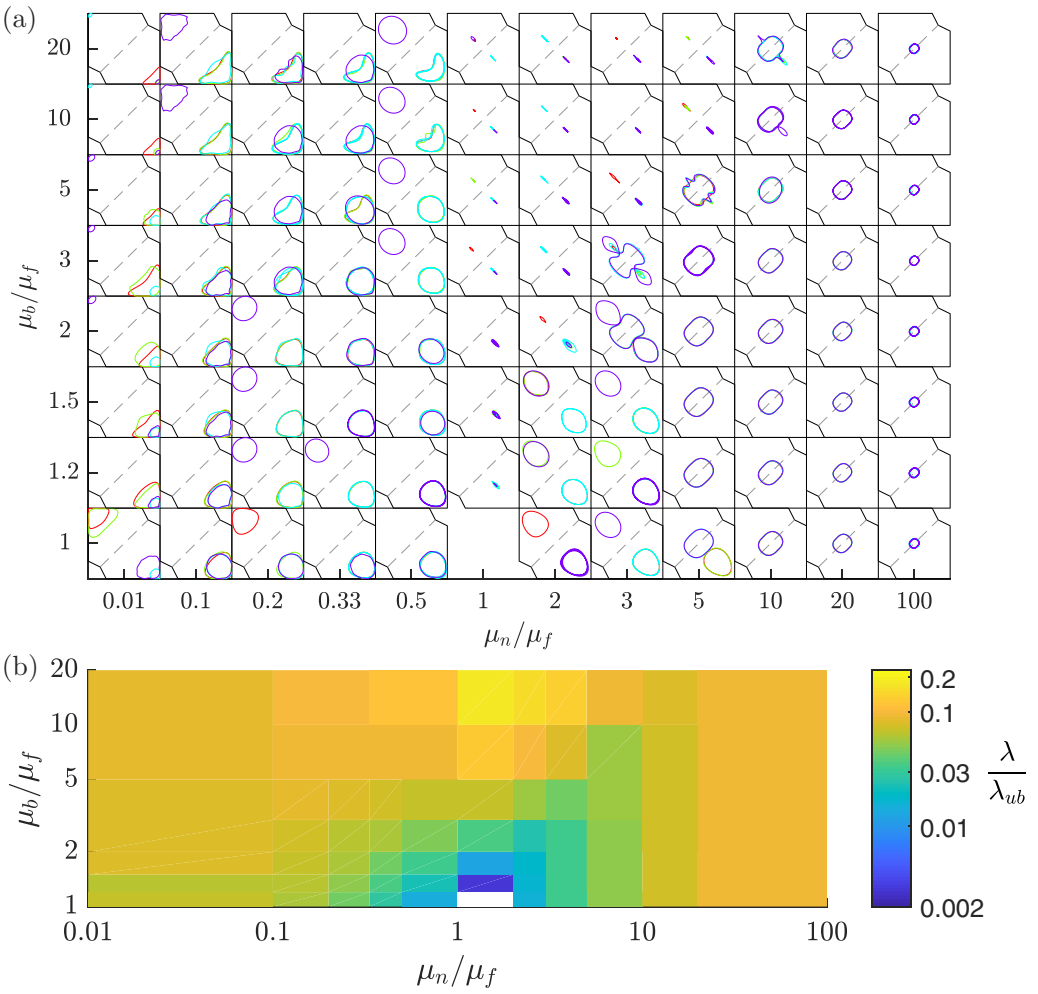

FIG. 14. (a) Trajectories (with bilateral or antipodal symmetry) that maximize relative efficiency, with different maximum harmonics k—3 (red), 5 (green), 7 (light blue), and 9 (purple)—when the resistance law is linear in velocity. (b) The relative efficiencies corresponding to the motions in panel (a).

Therefore,

$$\langle P\rangle \geqslant \mu_{\min}\int_0^1\int_0^1 \|\partial_t \mathbf{X}\|^2 ds\,dt = \mu_{\min}\int_0^1\int_0^1 \|\overline{\partial_t \mathbf{X}}\|^2 + \|\widetilde{\partial_t \mathbf{X}}\|^2 ds\,dt + 2\mu_{\min}\overline{\partial_t \mathbf{X}}\cdot\int_0^1\int_0^1 \widetilde{\partial_t \mathbf{X}}\,ds\,dt \tag{24}$$

$$= \mu_{\min}\int_0^1\int_0^1 \|\overline{\partial_t \mathbf{X}}\|^2 + \|\widetilde{\partial_t \mathbf{X}}\|^2 ds\,dt \geqslant \mu_{\min}\|\overline{\partial_t \mathbf{X}}\|^2. \tag{25}$$

Therefore, for a given average speed $\|\overline{\partial_t \mathbf{X}}\|$, $\langle P\rangle$ is at least $\mu_{\min}\|\overline{\partial_t \mathbf{X}}\|^2$, which occurs when all points of the body move uniformly in the direction of minimum resistance, at constant speed $\|\overline{\partial_t \mathbf{X}}\|$. This provides the upper bound on efficiency:

$$\lambda_{ub} \equiv \frac{1}{\mu_{\min}} \geqslant \frac{\|\overline{\partial_t \mathbf{X}}\|^2}{\langle P\rangle} = \lambda. \tag{26}$$

Figure 14(a) shows the trajectories (computed with the stochastic algorithm) that maximize relative efficiency, among the class of trajectories with either bilateral or antipodal symmetry, when the resistance law is linear in velocity. At large μ_n/μ_f, the trajectories are similar to those with Coulomb friction in Fig. 12. Near $\mu_n/\mu_f = 2$, the trajectories are off-center, like those in Fig. 11, and like that proposed by [5] for high efficiency, but those in Fig. 14 are rounder. At $\mu_n/\mu_f = \mu_b/\mu_f = 1$, all trajectories yield zero locomotion with linear resistance [37], so none is shown. For $\mu_b/\mu_f > 1$ and $\mu_n/\mu_f = 1$ and somewhat larger, small-amplitude reciprocal motions are optimal, similar to those in the sliding case, Fig. 11. The symmetrical lenticular or oval shapes in the central parts of Figs. 11 and 12 do not appear in Fig. 14. Here, rounded off-center trajectories appear at both $\mu_n/\mu_f >$ 1 and <1. Decreasing μ_n/μ_f to 0.1 and with $\mu_b/\mu_f > 1.5$, the trajectories become somewhat triangular, and very small in size as μ_n/μ_f is decreased further to 0.01, roughly like

those in Fig. 11, but not as small. In general, many of the optimal trajectories with linear resistance resemble those with the Coulomb friction resistance law. The differences are most pronounced in the vicinity of isotropic friction, where linear resistance yields no locomotion. Figure 14(b) shows the distribution of optimal relative efficiencies corresponding to panel (a). The distribution is similar to that of Fig. 13(b). The maximum occurs at the top center in both cases. Values decrease moving leftward and rightward, more to the right in Fig. 13(b) but more symmetrically in Fig. 14(b). The relative efficiency values are generally much lower for linear resistance—about 0–30% of the values for Coulomb friction in the left half of Fig. 13(b), $\mu_n/\mu_f < 1$. In the right half, they are also generally much lower, but they reach 50% of the Coulomb friction values when μ_n/μ_f increases to 10, and they exceed the Coulomb friction values by a few percent along the rightmost boundary, $\mu_n/\mu_f = 100$.

VI. SUMMARY AND CONCLUSIONS

We have investigated efficient sliding motions of three-link bodies with a Coulomb friction resistance law and various frictional anisotropy ratios. We found that the reduced space of elliptical (single-harmonic) trajectories gives a good representation of optimal motions when more harmonics are considered. Friction coefficient space can be partitioned into distinct regions (about seven are suggested here for elliptical trajectories) where different types of motions are optimal. Surprisingly, the top two elliptical optima usually belong to different clusters in trajectory coefficient space, despite having similar relative efficiencies, showing that very different motions can be close to optimal for a given choice of friction anisotropy ratios. Many of the elliptical optima bend symmetrically to either side of the flat state, but several optima are strongly asymmetrical, including small-amplitude reciprocal motions. Some of the optima resemble those seen previously in the smooth case—small-amplitude retrograde or direct wave locomotion with very large or very small normal friction, reciprocal (or ratcheting) motions with large backward friction. But most of the optima are distinct from those seen previously.

The elliptical motions with zero net rotation belong to three groups: those with a certain bilateral symmetry, antipodal symmetry, and a small subset of the reciprocal motions. For trajectories with harmonics up to a given integer, the first two groups have about half the dimension of general trajectories, but they achieve about the same maximum efficiency, with a noticeable reduction only for very small normal friction.

Adding the second or third harmonic to bilaterally symmetric elliptical trajectories increases the number of local optima by a factor of 4–8 in most of the parameter space, but increasing to about 20 when normal friction is small. Adding these modes increases the maximum efficiency by at most 50%, and usually much less. We then considered random ensembles with uniformly distributed coefficients of up to five harmonics. The probability density of efficiency has a peak at a nonzero efficiency in most cases, and falls off exponentially or faster up to the maximum efficiency value. Ensembles that include higher harmonics are skewed toward smaller efficiencies.

We developed a stochastic optimization method to find optimal trajectories in larger spaces of modes, with up to nine harmonics. We found rapid convergence with increasing numbers of modes. Bilaterally symmetric optima outperform antipodally symmetric optima where they differ. With small normal friction, the optimal trajectories with higher harmonics have the same general sizes and locations as the elliptical optima, but they have a triangular shape that increases efficiency by a factor as large as 6 at the smallest normal friction studied. At intermediate normal friction, the higher-harmonic optima are similar to the elliptical optima, though sometimes with angular shapes, and efficiencies are only moderately higher. In nearly all cases, the higher-harmonic optima are simple closed curves, even though simple closed curves are a small subset of the full set of trajectories (including those with self-intersection). With a linear resistance law, the peak relative efficiencies are much reduced, particularly near isotropic resistance where the efficiency is always zero. The optimal trajectories are similar to the Coulomb friction case at large normal friction, more off-center and rounded at moderate normal friction, and larger and more rounded triangular trajectories at very small normal friction. As with Coulomb friction, nearly reciprocal motions with very small amplitude predominate at large backward friction and moderate normal friction.

We mention as a possibility for future work the use of geometric techniques to visualize energy-optimal gaits by using the energy as a Riemannian metric [38,58]. Gaits (i.e., trajectories) that yield large displacements are those that enclose a large amount of an appropriately defined curvature quantity. A "gait gradient" can be computed that maximizes the net displacement of a gait subject to an energy constraint, and used to evolve the gait toward optimal efficiency.

ACKNOWLEDGMENT

This research was supported by the NSF Mathematical Biology program under Award No. DMS-1811889.

APPENDIX: COEFFICIENTS FOR ELLIPTICAL OPTIMA

Figure 15 shows the values of the three coefficients—A_0, A_1, and B_1—that define the top two local optimizers of efficiency among bilaterally symmetric ellipses, via Eq. (18). The left column [panels (a), (c), and (e)] shows the A_0, A_1, and B_1 values, respectively, for the top optimum. The mean shape is flat for $A_0 = 0$ and more folded as $|A_0|$ increases. The A_0 values in panel (a) are close to 0 (a nearly flat mean shape) in most cases, except for some very folded cases at the top, left of center [i.e., motion 8 in Fig. 4(d)], and at the bottom, right of center [i.e., motion 10 in Fig. 4(d)]. The amplitudes of the motions, described by A_1 [panel (c)] and B_1 [panel (e)] are typically close to 0 for $\mu_n/\mu_f \ll 1$, large for $\mu_n/\mu_f \approx 1$, and then very small again (for $\mu_b/\mu_f \gg 1$) or moderately small (for $\mu_b/\mu_f \approx 1$) when $\mu_n/\mu_f \geqslant 1$. There is more heterogeneity among the parameters for the second best optima [right column, panels (b), (d), and (f)]. By tracking the parameters of the top several optima (not shown beyond the top two) across friction coefficient parameter space, we have

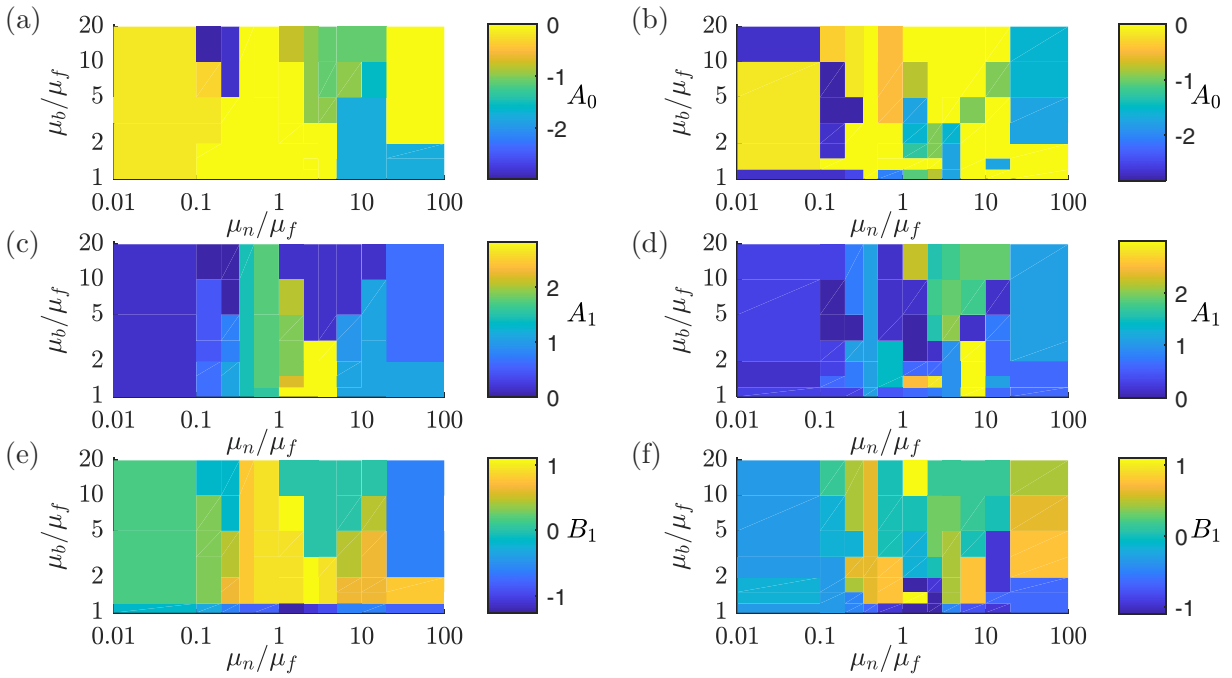

FIG. 15. The left column [panels (a), (c), and (e)] gives the values of the kinematic parameters A_0, A_1, and B_1, respectively, for the global optimizers of efficiency among elliptical trajectories with bilateral symmetry. The right column [panels (b), (d), and (f)] gives the same values for the second best local optimizers. The parameters are defined in (18) and shown in Fig. 3(b).

found that there are distinct branches of optima, with A_0, A_1, and B_1 values that change gradually as the friction coefficient ratios are varied. Their ordering by relative efficiency switches at certain friction coefficient ratios. This accounts for some of the sharp changes in the parameters of the first and second columns at certain friction coefficient values, where the best or second-best optima switch from one branch of optimal motions to another.

[1] E. M. Purcell, Life at low Reynolds number, Am. J. Phys **45**, 3 (1977).

[2] L. E. Becker, S. A. Koehler, and H. A. Stone, On self-propulsion of micro-machines at low Reynolds number: Purcell's three-link swimmer, J. Fluid Mech. **490**, 15 (2003).

[3] D. Tam and A. E. Hosoi, Optimal Stroke Patterns for Purcell's Three-Link Swimmer, Phys. Rev. Lett. **98**, 068105 (2007).

[4] J. E. Avron and O. Raz, A geometric theory of swimming: Purcell's swimmer and its symmetrized cousin, New J. Phys. **10**, 063016 (2008).

[5] O. Raz and J. E. Avron, Comment on "Optimal Stroke Patterns for Purcell's Three-Link Swimmer", Phys. Rev. Lett. **100**, 029801 (2008).

[6] R. L. Hatton, L. J. Burton, A. E. Hosoi, and H. Choset, Geometric maneuverability with applications to low Reynolds number swimming, in *Proceedings of the 2011 IEEE/RSJ International Conference on Intelligent Robots and Systems (IROS)* (IEEE, Piscataway, NJ, 2011), pp. 3893–3898.

[7] G. Huber, S. A. Koehler, and J. Yang, Micro-swimmers with hydrodynamic interactions, Math. Comput. Modell. **53**, 1518 (2011).

[8] E. Passov and Y. Or, Dynamics of Purcell's three-link microswimmer with a passive elastic tail, Eur. Phys. J. E **35**, 78 (2012).

[9] F. Alouges, A. DeSimone, L. Giraldi, and M. Zoppello, Self-propulsion of slender micro-swimmers by curvature control: N-link swimmers, Int. J. Non-Lin. Mech. **56**, 132 (2013).

[10] L. Giraldi, P. Martinon, and M. Zoppello, Optimal design of Purcell's three-link swimmer, Phys. Rev. E **91**, 023012 (2015).

[11] O. Wiezel and Y. Or, Optimization and small-amplitude analysis of Purcell's three-link microswimmer model, Proc. R. Soc. A **472**, 20160425 (2016).

[12] R. L. Hatton, T. Dear, and H. Choset, Kinematic cartography and the efficiency of viscous swimming, IEEE Trans. Rob. **33**, 523 (2017).

[13] P. Bettiol, B. Bonnard, L. Giraldi, P. Martinon, and J. Rouot, The Purcell three-link swimmer: Some geometric and numerical aspects related to periodic optimal controls, Radon Ser. Comput. Appl. Math. **18**, 314 (2017).

[14] E. Kanso, J. E. Marsden, C. W. Rowley, and J. B. Melli-Huber, Locomotion of articulated bodies in a perfect fluid, J. Nonlin. Sci. **15**, 255 (2005).

[15] F. Jing and S. Alben, Optimization of two- and three-link snake-like locomotion, Phys. Rev. E **87**, 022711 (2013).

[16] T. Yona and Y. Or, The wheeled three-link snake model: Singularities in nonholonomic constraints and stick–slip hybrid dynamics induced by coulomb friction, Nonlin. Dyn. **95**, 2307 (2019).

[17] G. I. Taylor, Analysis of the swimming of long and narrow animals, Proc. R. Soc. London A **214**, 158 (1952).

[18] L. J. Burton, R. L. Hatton, H. Choset, and A. E. Hosoi, Two-link swimming using buoyant orientation, Phys. Fluids **22**, 091703 (2010).

[19] S. E. Spagnolie, Rehinging biflagellar locomotion in a viscous fluid, Phys. Rev. E **80**, 046323 (2009).

[20] S. Alben and C. Puritz, Intermittent sliding locomotion of a two-link body, Phys. Rev. E **101**, 052613 (2020).

[21] S. Alben, Optimizing snake locomotion in the plane, Proc. R. Soc. A **469**, 20130236 (2013).

[22] F. L. Chernousko, Snake-like locomotions of multilink mechanisms, J. Vib. Control **9**, 235 (2003).

[23] F. L. Chernousko, Modelling of snake-like locomotion, Appl. Math. Comput. **164**, 415 (2005).

[24] F. Alouges, A. DeSimone, L. Giraldi, Y. Or, and O. Wiezel, Energy-optimal strokes for multi-link microswimmers: Purcell's loops and Taylor's waves reconciled, New J. Phys. **21**, 043050 (2019).

[25] D. L. Hu and M. Shelley, Slithering locomotion, in *Natural Locomotion in Fluids and on Surfaces* (Springer, New York, 2012), pp. 117–135.

[26] M. A. Shugen, Analysis of creeping locomotion of a snake-like robot, Adv. Rob.: Int. J. Rob. Soc. Jpn. **15**, 205 (2001).

[27] M. Sato, M. Fukaya, and T. Iwasaki, Serpentine locomotion with robotic snakes, IEEE Control Syst. Mag. **22**, 64 (2002).

[28] Z. V. Guo and L. Mahadevan, Limbless undulatory propulsion on land, Proc. Natl. Acad. Sci. USA **105**, 3179 (2008).

[29] D. L. Hu, J. Nirody, T. Scott, and M. J. Shelley, The mechanics of slithering locomotion, Proc. Natl. Acad. Sci. USA **106**, 10081 (2009).

[30] E. Lauga and T. R. Powers, The hydrodynamics of swimming microorganisms, Rep. Prog. Phys. **72**, 096601 (2009).

[31] H. B. Lillywhite, *How Snakes Work: Structure, Function and Behavior of the World's Snakes* (Oxford University Press, Oxford, 2014).

[32] P. Liljebäck, K. Y. Pettersen, Ø. Stavdahl, and J. T. Gravdahl, *Snake Robots: Modelling, Mechatronics, and Control* (Springer, London, 2012).

[33] A. M. Bloch, P. S. Krishnaprasad, J. E. Marsden, and R. M. Murray, Nonholonomic mechanical systems with symmetry, Arch. Ration. Mech. Anal. **136**, 21 (1996).

[34] R. L. Hatton, Y. Ding, H. Choset, and D. I. Goldman, Geometric Visualization of Self-Propulsion in a Complex Medium, Phys. Rev. Lett. **110**, 078101 (2013).

[35] R. L. Hatton and H. Choset, Geometric motion planning: The local connection, Stokes theorem, and the importance of coordinate choice, Int. J. Rob. Res. **30**, 988 (2011).

[36] J. Dai, H. Faraji, C. Gong, R. L. Hatton, D. I. Goldman, and H. Choset, Geometric swimming on a granular surface, in *Robotics: Science and Systems* (MIT Press, Cambridge, MA, 2016).

[37] S. Alben, Efficient sliding locomotion with isotropic friction, Phys. Rev. E **99**, 062402 (2019).

[38] S. Ramasamy and R. L. Hatton, Soap-bubble optimization of gaits, in *Proceedings of the 2016 IEEE 55th Conference on Decision and Control (CDC)* (IEEE, Piscataway, NJ, 2016), pp. 1056–1062.

[39] B. Bittner, R. L. Hatton, and S. Revzen, Geometrically optimal gaits: A data-driven approach, Nonlin. Dyn. **94**, 1933 (2018).

[40] R. G. Cox, The motion of long slender bodies in a viscous fluid. Part 1. General theory, J. Fluid Mech. **44**, 791 (1970).

[41] X. Wang, M. T. Osborne, and S. Alben, Optimizing snake locomotion on an inclined plane, Phys. Rev. E **89**, 012717 (2014).

[42] X. Wang and S. Alben, Dynamics and locomotion of flexible foils in a frictional environment, Proc. R. Soc. A **474**, 20170503 (2018).

[43] E. Gutman and Y. Or, Symmetries and gaits for Purcell's three-link microswimmer model, IEEE Trans. Rob. **32**, 53 (2015).

[44] J. McGarva and G. Mullineux, Harmonic representation of closed curves, Appl. Math. Model. **17**, 213 (1993).

[45] D. Pham and D. Karaboga, *Intelligent Optimisation Techniques: Genetic Algorithms, Tabu Search, Simulated Annealing and Neural Networks* (Springer Science & Business Media, 2012).

[46] T. Zhang and D. I. Goldman, The effectiveness of resistive force theory in granular locomotion, Phys. Fluids **26**, 101308 (2014).

[47] Z. Peng, Y. Ding, K. Pietrzyk, G. J. Elfring, and O. S. Pak, Propulsion via flexible flapping in granular media, Phys. Rev. E **96**, 012907 (2017).

[48] E. E. Keaveny and A. E. X. Brown, Predicting path from undulations for C. elegans using linear and nonlinear resistive force theory, Phys. Biol. **14**, 025001 (2017).

[49] O. Schnitzer and E. Yariv, Resistive-force theory for mesh-like superhydrophobic surfaces, Phys. Rev. Fluids **3**, 032201(R) (2018).

[50] C. E. López and E. Lauga, Hydrodynamic model for spiroplasma motility, Phys. Rev. Fluids **5**, 093102 (2020).

[51] N. Cohen and J. H. Boyle, Swimming at low Reynolds number: A beginners guide to undulatory locomotion, Contemp. Phys. **51**, 103 (2010).

[52] E. E. Riley and E. Lauga, Empirical resistive-force theory for slender biological filaments in shear-thinning fluids, Phys. Rev. E **95**, 062416 (2017).

[53] A. M. Leshansky, Enhanced low-Reynolds-number propulsion in heterogeneous viscous environments, Phys. Rev. E **80**, 051911 (2009).

[54] P. Sauvage, M. Argentina, J. Drappier, T. Senden, J. Siméon, and J.-M. Di Meglio, An elasto-hydrodynamical model of friction for the locomotion of Caenorhabditis elegans, J. Biomech. **44**, 1117 (2011).

[55] X. N. Shen, J. Sznitman, P. Krajacic, T. Lamitina, and P. E. Arratia, Undulatory locomotion of Caenorhabditis elegans on wet surfaces, Biophys. J. **102**, 2772 (2012).

[56] Y. Rabets, M. Backholm, K. Dalnoki-Veress, and W. S. Ryu, Direct measurements of drag forces in C. elegans crawling locomotion, Biophys. J. **107**, 1980 (2014).

[57] J. Lighthill, *Mathematical Biofluiddynamics* (SIAM, Philadelphia, 1975).

[58] S. Ramasamy and R. L. Hatton, The geometry of optimal gaits for drag-dominated kinematic systems, IEEE Trans. Rob. **35**, 1014 (2019).